Identification of iron in Earth analogues of Martian phyllosilicates using visible reflectance spectroscopy: spectral derivatives and color parameters

Manuel Sánchez-Marañón [a], Javier Cuadros [b], Joseph R. Michalski [c], Manuel Melgosa [d], Vesselin Dekov [e]

[a] Department of Soil Science and Chemical Agriculture, University of Granada, 18071 Granada, Spain

[b] Department of Earth Sciences, Natural History Museum, Cromwell Road, London SW7 5BD, UK

[c] Department of Earth Sciences & Laboratory for Space Research, The University of Hong Kong, Hong Kong, China

[d] Department of Optics, University of Granada, 18071 Granada, Spain

[e] Department of Marine Resources and Energy, Tokyo University of Marine Science and Technology, 4-5-7 Konan, Minato-ku, Tokyo 108-8477, Japan

Corresponding author: msm@ugr.es

Abstract

A range of phyllosilicate compositions have been detected spectroscopically on Mars, but the largest fraction by far corresponds to clay minerals rich in Fe and Mg. Given that most of our understanding of Martian clays comes from remote sensing data, it is critically important to explore the details of how compositional variation affects spectral features of phyllosilicates. The greatest efforts have focused so far on near-infrared (NIR) spectroscopy. Recently, ambiguities have been detected in the NIR spectra of 2:1 phyllosilicates with intermediate Fe-Mg content that preclude mineral and chemical discrimination. Such ambiguities highlight the relevance of exploring the visible spectral range as a complementary tool to characterize Martian phyllosilicates precisely. This article reports the investigation of laboratory reflectance spectra (330-800 nm) from 34 Earth analogues of Martian phyllosilicates with a wide range of Mg-Fe composition, including nontronite, celadonite and saponite end-members, as well as interstratified glauconite-nontronite, talc-nontronite, and talc-saponite. The spectra indicated the presence of Fe^{3+} by absorption modulations and a decrease in total reflectance, especially in samples with tetrahedral Fe^{3+}. Absorption bands at 370 and 420 nm were diagnostic of octahedrically and tetrahedrally coordinated Fe^{3+}, respectively. Band amplitudes in the second derivative of the Kubelka-Munk function correlated positively with Fe^{3+} content ($R^2 > 0.8$). Standard color analyses of the visible reflectance spectra under the CIE illuminant D65 indicated that the CIELAB color parameter a^*_{10} was positively correlated with tetrahedral Fe^{3+}, b^*_{10} was positively correlated with octahedral Fe^{3+}, and L^*_{10} was negatively correlated with Fe^{3+} in both structural sites. Because Fe^{2+} was in relatively low amount, it did not provide clear spectral evidence. Multiple regression models using the amplitude of the diagnostic absorption bands predicted well absolute Fe content in the phyllosilicates ($R^2 = 0.89$) and the ratio Fe/(Fe+Mg+Al) ($R^2 = 0.84$). CIELAB color parameters improved the prediction of total Fe ($R^2 = 0.92$) and the ratio Fe/(Fe+Mg+Al) ($R^2 = 0.93$). Application of these analyses to Martian data has challenges set by Fe oxide dust coating and spatial and spectral resolution. However, these results mark an avenue to develop testable tools using visible-wavelength spectral data from both satellite

and lander probes to help establishing Fe content and mineral identification of Martian phyllosilicates.

Keywords: Color, Fe content, Mars, Phyllosilicates, Visible spectral range

1. Introduction

Clay minerals formed by alteration of mafic rocks have variable amounts of Fe whose determination is important for their mineralogical and chemical characterization. Reflectance spectroscopy is a technique increasingly used because it allows remote-sensing identification and characterization of mineral deposits both on Earth and in planetary bodies, including ferromagnesian phyllosilicates (Blewett et al., 1995; Moroz et al., 2000; Fan et al., 2012; Carter et al., 2013, Schäfer et al., 2016). Particularly, the near-infrared range (NIR) has been used with tremendous success in Mars exploration, where abundant phyllosilicate deposits have been identified. Very succinctly, phyllosilicates are identified and characterized with NIR spectroscopy using mainly the following absorption bands: one at 1.9 μm, indicating the existence of hydration water (a typical feature of fine-grained phyllosilicates), and bands of variable position around 1.4 μm and between 2.18 and 2.35 μm, corresponding to hydroxyl vibrations that change frequency depending on the crystal-chemical environment of hydroxyl groups in the phyllosilicates (Bishop et al., 2008a). In addition, hydration water also contributes a component to the 1.4 μm band (Bishop et al., 1994). So far, remote-sensing identification of the Martian phyllosilicates is based mainly on the comparison between spectra of phyllosilicate end-members from libraries and Martian spectra. The shortcomings of such an approach are obvious, because it can be expected that Martian phyllosilicates will frequently have complex, intermediate compositions or appear in polymineralic mixtures. Efforts are being carried out to increase our ability to characterize Martian phyllosilicate phases with a wider or more complex range of chemical and structural features (Milliken et al., 2010; McKeown et al., 2011; Cuadros and Michalski, 2013).

In particular, correlations between the octahedral chemistry and the position and intensity of NIR hydroxyl bands have been carefully investigated in the Mg-Fe compositional range, including nontronite and interstratified glauconite-nontronite, talc-nontronite, and talc-saponite (Michalski et al., 2015; Cuadros et al., 2016). Authors concluded that substitution of both Fe^{3+} for Al and that of

divalent cations for trivalent cations in dioctahedral phyllosilicates clearly displace the vibration of hydroxyl bands to longer wavelengths, but that no band modification accompanies Fe^{3+} substitution for Mg in trioctahedral clays, which means that Fe detection and phyllosilicate identification with NIR is unreliable in this latter case. Further, Fe-Mg phyllosilicates with a mixed dioctahedral and trioctahedral composition (talc-nontronite, saponite-nontronite) cannot be distinguished from nontronite. It is then desirable to develop complementary analyses that may help to discriminate chemistry and mineralogy where NIR cannot.

In the visible spectral region there are also diagnostic features of the presence of Fe in minerals, which have been explained using the crystal field theory (Burns, 1993). In particular, Sherman and Vergo (1988) provided detailed absorption band assignments of electronic transitions to assist interpretation of spectra from nontronites and other Fe-containing smectites. Their visible spectra were dominated by the crystal field transitions of Fe^{3+} in octahedral coordination sites such as the $2[^6A_{1g}] \rightarrow 2[^4T_{1g}]$ transition, that produces an absorption band near 22000 cm^{-1} (455 nm), attributed to electron-pair excitation of magnetically coupled Fe^{3+} cations. Other important octahedral Fe^{3+} transitions found by Sherman and Vergo (1988) were $^6A_{1g} \rightarrow {}^4T_{2g}$ and $^6A_{1g} \rightarrow {}^4E_g$, producing, respectively, bands at 15500 cm^{-1} (645 nm) and 27000 cm^{-1} (370 nm). In addition, an absorption band around 23000 cm^{-1} (435 nm) was assigned to the $^6A_1 \rightarrow {}^4E, {}^4A_1$ single-electron transition of tetrahedrally coordinated Fe^{3+}. In this case, the electronic transition is Laporte-allowed, which means a much greater absorption coefficient than for transitions of octahedrally coordinated Fe^{3+}. One more band described by Sherman and Vergo (1988) was that at 14000-15000 cm^{-1} (666-714 nm) in a saponite and a montmorillonite, that they assigned to intervalence charge transfer $Fe^{2+} + Fe^{3+} \rightarrow Fe^{3+} + Fe^{2+}$. Intervalence charge transfer has also been described near 13700 cm^{-1} (730 nm) in the spectrum of a reduced nontronite (Lear and Stucki, 1987). The high intensity of the 435 nm band of tetrahedrally coordinated Fe^{3+} is illustrated by the fact that the existence of such absorption band made a saponite dark brown rather than green, as expected for a mixed-valent saponite with

101 Fe^{2+} and Fe^{3+} in octahedral coordination (Sherman and Vergo, 1988). Indeed, color in minerals is
102 mainly controlled by absorptions in the visible wavelength range, although is also modified by other
103 factors such as particle size and surface roughness (Burns, 1993; Sánchez-Marañón et al., 2004).
104
105 There is widespread use of the visible spectral range in the identification and quantification of Fe
106 oxides, oxy-hydroxides, and hydroxy-sulfates by examining the shape of diffuse-reflectance spectra
107 (Bishop and Murad, 1996), analyzing the position and intensity of the crystal field bands (Sánchez-
108 Marañón et al., 2015), and calculating color parameters (Scheinost and Schwertmann, 1999; Torrent
109 and Barrón, 2002; Sellitto et al., 2009). The successful application of visible spectroscopy to Fe
110 oxides and oxy-hydroxides, with structural similarities to phyllosilicates, suggests that the same
111 approach is viable for the latter. Indeed, the absorption bands of octahedral Fe^{3+} in nontronite have
112 similar wavelengths to those of the ferric oxides and oxy-hydroxides (Sherman and Waite, 1985;
113 Scheinost et al., 1998). One may expect color to be a diagnostic and quantifiable feature of the
114 amount and position of Fe^{3+} in phyllosilicates.
115
116 The reliability of visible spectroscopy and colorimetric methods to investigate Fe in phyllosilicates
117 is finding confirmation. A plethora of research articles on the mineralogy of planetary materials and
118 Earth analogs has addressed the interpretation of extended visible-region spectra (400-1000 nm),
119 although most of these were concerned with finding a set of spectral indices of chemical and
120 mineralogical composition without colorimetric meaning (Morris et al., 2000; Farrand et al., 2008;
121 Schäfer et al., 2016). Further to this, the chromophore effect of Fe structurally bound in clay
122 minerals, which reduces their brightness (Mussel et al., 2008), is well-known, and a number of
123 studies have proved the merit of colorimetry in identifying the presence of Fe in phyllosilicates with
124 minor and trace contents. Quantitative analyses of the color of clays using a standard observer and a
125 standard illuminant in the CIELAB color space (CIE, 2004), showed inverse correlations ($P <$
126 0.001) of the Fe^{3+} content with L^*_{10} (lightness) and $h_{ab,10}$ (hue-angle), as well as positive

127 correlations with a^*_{10} and b^*_{10} (chromatic coordinates) in talc (Soriano et al., 1998; Soriano et al.
128 2002) and kaolinite (Gámiz et al., 2005; Gámiz et al., 2011; Bouzidi et al., 2014).
129
130 The objective of the current study was to analyze the visible-region reflectance spectra of 2:1
131 phyllosilicates with a wide range of chemical composition and complex structural features, from
132 nontronite and glauconite to talc and saponite, both end-member and interstratified phases, in order
133 to evaluate their Fe content using crystal-field band positions and color parameters. The results of
134 this study are of particular interest for investigation of phyllosilicates on Mars, as they may provide
135 alternative and complementary evidence to remote-sensing NIR and chemical and mineralogical
136 techniques in landers.
137
138 **2. Samples and methods**
139 Thirty four samples were investigated, consisting of the following end-member and interstratified
140 phyllosilicates: nontronite, celadonite, saponite, glauconite-nontronite, talc-nontronite, and talc-
141 saponite (Table 1). Four samples are of continental origin (Glauconite 97, Nontronite 33B,
142 Nontronite 51, and CRB 03-026; hereinafter named continental samples), whereas the rest
143 originated in submarine hydrothermal fields. Their specific origin, determination and discussion of
144 their mineralogy, chemical composition, and crystal-chemical structure are in Cuadros et al. (2013).
145 Their results are summarized in Table 1. The samples cover a range of Mg-Fe chemical
146 composition in the mineral series talc/saponite (Mg-rich) to celadonite/nontronite/glauconite (Fe-
147 rich). They were investigated as proxies for the Mg/Fe-rich smectitic phyllosilicates found on Mars
148 (Michalski et al., 2015; Cuadros et al., 2016). Some of the samples contain two or more
149 phyllosilicate phases, both end-members and interstratified phases (e.g., sample M64/1 139GTV-
150 5E [Turtle pits] contains three talc-saponite phases and one saponite end-member).
151

The clay samples were ground manually in an agate mortar during 10 min until a fine, homogeneous powder was obtained. Approximately 100 mg of each sample were prepared as a loose powder in a 1-cm diameter sample cup under ambient air atmosphere. The spectral reflectance factor from each sample was recorded using a bi-directional spectrometer at Reflectance Experiment Laboratory (RELAB, Brown University, Rhode Island, U.S.A.) in the 330-2540 nm range at a resolution of 10 nm. The bi-directional reflectance factor is defined as the ratio of the radiant flux reflected by the sample surface to that reflected in identical conditions by a standard nearly-Lambertian diffusing surface with reflectance close to 100% (Baumgardner et al., 1985). Bi-directional reflectance measurements usually have the contribution of both specular and diffuse reflectance, however, the small particle size and rough surface (loose packing) of the samples minimized the specular contribution. The measurements were carried out using an incident beam at 30º and a reflected beam at 0º from the normal to the sample surface. The sample cup was rotated during the analysis. A quartz halogen lamp was used as the light source and pressed Halon as the standard diffusing surface. We selected the spectral range 330-800 nm to analyze the standard visible range (380-780 nm according to CIE, 2004) and its near surroundings.

We first compared the shape of the spectral curves (reflectance factors *vs.* wavelength values) and their intensity. Second, we investigated the second derivative of the absorption (not reflectance) spectra from the samples in order to locate the absorption band positions with higher accuracy. For this, from the values of reflectance factors R, we calculated the Kubelka–Munk function $K/S = (1-R)^2/2R$ (Eq. 1), which determinates the ratio of absorption (K) to scattering (S) at different wavelengths. Assuming that the scattering coefficient has only a small variation with wavelength over the range of interest, the K/S curve can be used as an absorption spectrum (Sherman and Waite, 1985). The second derivatives of the K/S data were calculated using the OriginPro v. 7.5 software (OriginLab Co, MA). Spectral filtering with the Savitzky-Golay method (Savitzky and Golay, 1964) significantly reduced high frequency noise without degrading the shape of the

derivative spectra. This method smoothes the second-derivative curve by performing a local polynomial regression around each point. We used 5th-order polynomial curves that included 5 points of the curve in each local polynomial regression. The second derivative enhances the resolution of *K/S* curves and the position and intensity of the absorption bands are more easily determined. The absorption bands appear as minimum values in the Kubelka-Munk second-derivative curves. To obtain an intensity index of each band, we used the amplitude (A) between its minimum value (center of the band) and maximum subsequent value (Scheinost et al., 1998).

Finally, from the measured spectral reflectance factors *R* between 380 and 780 nm, we calculated the CIELAB color parameters L^*_{10}, a^*_{10}, b^*_{10}, $C^*_{ab,10}$, and $h_{ab,10}$ for each sample, using the equations provided by the International Commission on Illumination (CIE), assuming the CIE D65 illuminant (artificial *daylight* with a correlated color temperature of 6500 K) and the CIE 1964 standard colorimetric observer (numerical description of the average human eye's color response), as recommended at CIE (2004). Although these parameters will not represent the colors observed anywhere on Earth or Mars, because of the multiple light variations caused by the composition and conditions of the corresponding atmospheres (Sánchez-Marañón et al., 2011), the assumption of D65 illuminant and CIE 1964 observer is a CIE standard procedure that allows coherent parameterization of color. The CIELAB parameters represent color as a vector from a set of normal three-dimensional coordinates. The parameter L^*_{10}, designated as *lightness*, represents the achromatic perception in a grey scale ranging from 0 (black) to 100 (white). The parameters a^*_{10} and b^*_{10} are the *chromatic coordinates* and they represent the amount of red ($+a^*_{10}$) or green ($-a^*_{10}$), and the amount of yellow ($+b^*_{10}$) or blue ($-b^*_{10}$) in a given color. Alternatively, the parameters a^*_{10} and b^*_{10} can be substituted by *hue-angle* ($h_{ab,10}$) and *chroma* ($C^*_{ab,10}$), which are polar coordinates (CIE, 2004). $C^*_{ab,10}$ is the relative strength of a color, measured as the length of the projection of the color vector on the $a^*_{10}b^*_{10}$ plane (perpendicular to the L^*_{10} coordinate), and $h_{ab,10}$ is the angle between the vector projected on the $a^*_{10}b^*_{10}$ plane and the $+a^*_{10}$ axis.

Pearson's correlation and regression analyses between Fe content from chemical data of Cuadros et al. (2013) (Table 1), the band amplitudes of the second derivatives of the Kubelka-Munk spectra, and the calculated CIELAB color parameters were performed with Statgraphic Centurion XVI (Statpoint Technologies, Inc., Warrenton). The data distributions were first tested for normality. Multiple linear-regression models for the prediction of Fe content (Table 1) from spectral data were constructed by using the forward stepwise analysis. The entry of variables into the models was controlled by an F-ratio criterion of 4 (Schabenberger and Pierce, 2002).

Several remote-sensing images and spectra from Mars were used to discuss the application of the above spectral analysis to Martian data. Three HiRISE (High Resolution Imaging Science Experiment) images were used from the following areas of Mars: Mawrth Vallis (image PSP_006742_2050; two parts of this image were used), Nili Fossae (image ESP_040113_1995) and Eridania basin (image ESP_012945_1450). The visible-range spectra of these three HiRISE images were also used. CRISM (Compact Reconnaissance Imaging Spectrometer for Mars) visible and NIR spectra from Marwth Vallis were used from the image FRT000094f6.

3. Results

3.1. Reflectance spectra

The shape of reflectance spectra was qualitatively well correlated with the clay mineralogy (Figure 1). Nontronite, talc-nontronite (T-N), and glauconite-nontronite (G-N) samples had low reflectance at short wavelength; the reflectance increased in the range from 380 to 500 nm (wavelengths corresponding to blue), followed by a peak or change of slope (shoulder) at ~580 nm. This wavelength corresponds to reflectance of green. From 580 nm to longer wavelengths, moving into yellow and red, the reflectance progressively increased in nontronite (Figure 1a) and T-N samples (Figure 1c) but it dropped in the G-N samples (Figure 1b). The two continental samples, Nontronite

33B and the T-N Nontronite 51 (with 24% of interstratified talc, Table 1) had greater reflectance values throughout the spectrum and more reflectance modulations below 500 nm than submarine nontronite and T-N (Figure 1a,c). Subtle differences were also observed between the spectra of the continental glauconite (Glauconite 97), that has little nontronite (4% layers, Table 1), and the rest of G-N samples of submarine hydrothermal origin, all of which contain greater nontronite concentration (23-68% layers, Figure 1b). In the latter group the maximum reflectance was at 580 nm, whereas for the continental glauconite was at 560 nm. Continental celadonite with 25% of saponite (CRB 03-026) had a similar spectrum to those of T-N (Figure 1c). Spectra of the submarine samples of the talc-saponite (T-S) group (Figure 1d) had a more or less continuous increase of reflectance from 380 to 800 nm, although a few samples showed spectral modulations, mainly at 500-600 nm. The total reflectance of the spectra in this group was very variable.

The group of G-N spectra is the most homogeneous in shape and reflectance factor (Figure 1). The spectral differences between continental and submarine samples in the nontronite and T-N groups (Figure 1a,c) may be related to the lack of tetrahedrally coordinated Fe^{3+} in samples with a continental origin (Nontronite 33B and Nontronite 51, Table 1). Within the T-S group, those samples with spectral modulations also had a relatively larger Fe^{3+} content (Figure 1d and Table 1), whereas samples with low Fe/Mg ratios (Table 1) were characterized by a greater total reflectance, especially at 600-800 nm (Figure 1d). Finally, the spectra of samples with interstratified T-N (Figure 1c), which have intermediate dioctahedral-trioctahedral composition and abundant Fe and Mg (Table 1), were similar to submarine nontronite spectra (Figure 1a), suggesting the predominant influence of Fe^{3+} in shaping these spectra. In summary, the main controls of light absorption in the samples seem to be Fe^{3+} content and location in the crystal lattice.

3.2. Second derivative of absorption spectra

The analysis of the second derivative of the Kubelka-Munk spectrum (or absorption spectrum) allows the detailed investigation of spectral absorption bands. The positions of the minima (absorption maxima) of the second-derivative of *K/S* calculated with the Kubelka-Munk function were similar for most samples (Figure 2). The spectra showed two well defined absorption bands, one near the lower limit of the visible region at 370 nm and another at 420 nm, as well as a broader band centered near 500 nm (position between 490 and 520 nm; Figure 2). According to the assignments of Sherman and Vergo (1988) described in the introduction section, the minima in the second derivative spectra of our samples at 370 and ~500 nm could be produced by Fe^{3+} in an octahedral field, whereas the band at 420 nm would result from Fe^{3+} in tetrahedral coordination.

The band at 420 nm did not appear in the two continental samples Nontronite 33B and Nontronite 51 (Figure 2a,c), which have no tetrahedral Fe^{3+} (Table 1). In addition, these two samples had the absorption band of octahedral Fe^{3+} at ~450 nm, rather than 490-500 nm, in better agreement with the position found by Sherman and Vergo (1988) for other continental nontronites (~22000 cm^{-1} or 455 nm). As the submarine nontronite (Figure 2a) and T-N (Figure 2c) samples all have tetrahedral Fe^{3+}, the assignment of the 420 nm band to tetrahedral Fe^{3+} is confirmed. Further, in the continental Nontronite 33B and Nontronite 51 there was no band at 370 nm but at 380 nm, and with low intensity (especially in Nontronite 51).

Most nontronite and G-N spectra had a weak and broad absorption band near 650 nm (Figure 2a,b), probably due mainly to additional transitions in octahedral Fe^{3+} (645 nm) but perhaps also to $Fe^{2+} \rightarrow Fe^{3+}$ charge transfer (666-714 nm) (Sherman and Vergo, 1988). The proximity of absorption bands from these two assignments and the poor definition of the band in the second derivative spectra prevents its precise attribution. Finally, the T-S samples had low-intensity second-derivative minima (Figure 2d), in agreement with their lower Fe content. Although there was significant Fe^{2+} content in some T-S samples (as determined from Mössbauer spectroscopy, Table 1), there was no

band that could be assigned exclusively to this reduced Fe form (there is the possibility of $Fe^{2+} \rightarrow Fe^{3+}$ charge transfer, as indicated above).

The band intensities in the second-derivative curves were measured using the amplitude of the peak from the ~370 nm minimum to the following maximum at ~400 nm; the amplitude from the ~420 nm minimum to the next maximum at ~450 nm; and from the ~500 nm minimum to the next maximum at ~560 nm. These three amplitudes are referred as $A_{370\text{-}400}$, $A_{420\text{-}450}$, and $A_{500\text{-}560}$, respectively. The samples Nontronite 33B (green spectrum in Figure 2a) and Nontronite 51 (red spectrum in Figure 2c) were not used in the calculation of $A_{370\text{-}400}$ and $A_{420\text{-}450}$ because they lacked these bands (Figure 2), as indicated above. In addition, the overall shape of their second-derivative spectra were different, as their most prominent feature was not the minimum value corresponding to the ~370 nm band, but a maximum positive value at ~360 nm. Also, their bands at ~500 nm appeared little developed and displaced from the position in the bulk of the spectra, and thus these two samples were also omitted in the $A_{500\text{-}560}$ analysis.

The amplitude measurements were strongly correlated with the Fe content of the samples, as indicated by the coefficients of determination (R^2) of the regression models (Figure 3). More specifically, $A_{370\text{-}400}$ and $A_{500\text{-}560}$ were correlated with octahedral Fe^{3+}, whereas $A_{420\text{-}450}$ did with tetrahedral Fe^{3+}. Thus, there was further support for the assignment of the bands to octahedral and tetrahedral Fe^{3+} by Sherman and Vergo (1988), although some of the band positions did not exactly match those indicated by these authors. The regression equations of $A_{370\text{-}400}$ and $A_{420\text{-}450}$ with total Fe^{3+} content were also highly significant (R^2 = 0.83-0.86), most probably because, in our samples, the contents of octahedral and tetrahedral Fe^{3+} were positively correlated (r = 0.78, $P < 0.05$, n = 34). $A_{500\text{-}560}$ had the lowest correlation with total Fe^{3+}, which is consistent with the lower intensity and definition of the absorption band near 500 nm (Figure 2). Finally, the relations between band amplitudes and total Fe were as good as with Fe^{3+}, indicating the relative low contribution of Fe^{2+} to

the total amount of Fe (on average 6%, n = 34). Given that octahedral and tetrahedral Fe^{3+} contents were well correlated with, respectively, $A_{370\text{-}400}$ and $A_{420\text{-}450,}$ the combination of these two measurements predicted total Fe content (Figure 4a) and total Fe^{3+} content (not shown) with equal and great accuracy. When applying this correlation to unknown samples in order to predict their Fe content from their spectral data, it will be easier to use cation ratios rather than Fe content in the structural formula. For this reason, the multiple regression was also developed for the ratio Fe/(Fe+Mg+Al) (Figure 4b).

3.3. Clay color

This section describes numerically the colors of the 34 samples in the CIELAB color space, under the standardized experimental conditions of CIE illuminant D65 and CIE 1964 observer (Table 2). The main variation in the color of samples corresponded to lightness, with L^*_{10} values between 29.27 (darkest) and 85.84 (lightest). Although the chromatic coordinate a^*_{10} presented lower values (-6.18 to 12.79) than b^*_{10} (4.37 to 32.71), their variations generated a wide range of hue-angles from reddish ($h_{ab,10}$ = 56.59º) to greenish (124.15º) passing through a yellowish hue-angle (near 90º), which is by far the predominant hue in the samples. The chroma parameter, $C^*_{ab,10}$, ranged 5.28-33.29. In order to visualize the distribution of the three CIELAB coordinates a^*_{10}, b^*_{10}, and L^*_{10}, the samples were represented in a casement scatter plot for different L^*_{10} levels (Figure 5). By comparing this plot with Table 1, it can be seen that the arrangement of samples in Figure 5 did not exactly represent Fe content and its location in the structure of the phyllosilicates but, roughly, indicated that: (1) lightness (L^*_{10}) increased with decreasing Fe, except in the case of the two continental samples Nontronite 33B and Nontronite 51; (2) the amount of yellow (b^*_{10}) increased with Fe^{3+}; and (3) the amount of red (a^*_{10}) increased with tetrahedral Fe^{3+} content, all of which suggests that the amount of Fe^{3+} could be the most influential variable on the CIELAB color parameters of these clays. These interpretations were supported by a statistical analysis based on variable correlations including all CIELAB parameters and Fe content variables (Table 3). The

amount of Fe^{2+} was not significantly ($P < 0.05$) correlated with CIELAB color parameters. Lightness L^*_{10} was inversely correlated with Fe^{3+}, regardless of its position in the tetrahedral or octahedral sheet. The parameters a^*_{10} and $h_{ab,10}$ (inversely correlated to each other) were correlated with tetrahedral Fe^{3+}, whereas b^*_{10} and $C^*_{ab,10}$ did mainly with octahedral Fe^{3+}. On average, 80% of the total Fe was octahedrally coordinated Fe^{3+}, which is the reason why total Fe had a higher positive correlation with b^*_{10} and $C^*_{ab,10}$ than with a^*_{10} and $h_{ab,10}$ (the correlation coefficient of Total Fe and $h_{ab,10}$ was not significant at $P < 0.05$ [$r = -0.24$] and, therefore, is not listed in Table 3).

A multiple regression model using the CIELAB color parameters predicted with high accuracy both Fe content in the structural formula (Figure 6a) and the relative proportion Fe/(Fe+Mg+Al) in the studied phyllosilicates (Figure 6b). Iron content in both regressions was mainly dependent on L^*_{10} and b^*_{10}. These variables, L^*_{10} and b^*_{10}, explained 90% and 86% of the variation of total Fe and Fe/(Fe+Mg+Al), respectively, indicating an increase in the Fe content with increasing darkness (lower L^*_{10}) and yellow chromaticity (greater b^*_{10}) in the samples. The input of a^*_{10} (red chromaticity) in the regression model only explained 2% and 7% of the variation of the dependent variable and its interpretation is complex. Considering that tetrahedral Fe^{3+} was positively correlated with a^*_{10} (Table 3) and that tetrahedral Fe^{3+} and total Fe were also positively correlated (Table 3), one would expect that the model would involve an increase of a^*_{10} with increasing Fe content. This was not the case, however. Two reasons can be advanced now for this result. One, because the variations generating the two correlations above do not take place in the same samples. Second, because a^*_{10} has negative values in some cases (whereas all other parameters are always positive, Table 2) and this affects the sign of the corresponding coefficient in the equations of Figure 6. This question will be further discussed in the following section. If the parameter a^*_{10} is not included in the correlations, the resulting equations are the following: Total Fe = 1.85 - 0.038 L^*_{10} + 0.078 b^*_{10}, $R^2 = 0.90$, and Fe/(Fe+Mg+Al) = 0.678-0.014 L^*_{10} + 0.031 b^*_{10}, $R^2 = 0.86$.

4. Discussion

4.1. Evaluation of the results

The two types of analysis performed were able to produce physically meaningful results and predict Fe content in the samples. Overall, the analysis with the CIELAB parameters was more successful for two reasons. First, this analysis could incorporate all samples, whereas the investigation of the second derivative of the Kubelka-Munk equation could not incorporate Nontronite 33B and Nontronite 51. In these two samples the bands at 370 and 420 nm were replaced by bands at higher wavelengths, and the second-derivative spectra had a clearly different shape (Figure 2a,c). From the assignments of Sherman and Vergo (1988) it is deduced that the 420 nm band is absent in Nontronite 51 and 33B because of their lack of tetrahedral Fe^{3+}. Instead, the 450 nm band due to octahedral Fe^{3+} was observed. We have no information to interpret the replacement of the 370 nm band by the 380 nm band. In any event, these results indicate that phyllosilicates have structural and compositional modifications causing spectral variations that may hinder the universal applicability of this analysis. It is hoped that progress in the understanding of how the spectral modifications are generated will eliminate this difficulty. At this point, the CIELAB parameter approach appears as more generally applicable.

In the second place, the color investigation produced correlation equations that predicted Fe content better than the second-derivative approach (Figures 4 and 6). At the upper range of Fe abundance, the color analysis produced very accurate Fe content results, and showed a good sensitivity to Fe content (Figure 6). The second-derivative analysis, however, had low sensitivity in this area, with data points of similar observed Fe content spreading over a wide range of predicted values (Figure 4). In the lower half of Fe abundance values, both analyses performed more similarly, with a clear loss of sensitivity of the color approach with respect to the upper Fe content range.

384 The CIELAB color parameter analysis has a weakness due to the ambiguous contribution of the
385 parameter a^*_{10}. This parameter has a negative coefficient in the equations predicting Fe content in
386 the samples (Figure 6), which appears as counterintuitive. The parameter a^*_{10} (red chromaticity)
387 increases with tetrahedral Fe (Table 3). In our samples, tetrahedral Fe and total Fe contents have a
388 weak positive correlation (Table 3). It may seem logical to assume that, generally, these two values
389 will be positively correlated in phyllosilicates. Interestingly, however, Kaufhold et al. (2017)
390 investigated nine smectites from bentonites with the range of Fe content 1.2-11.0 wt% Fe_2O_3 and
391 found no correlation between total and tetrahedral Fe. According to the Fe content in these
392 smectites, none of them was a nontronite. Rather, they were in the range montomorillonite to Fe-
393 rich montmorillonite. Nonetheless, the correlation between total and tetrahedral Fe appears to
394 develop where the Fe content is high. Thus, Gates et al. (2002) determined values from 14
395 nontronites, where they found a threshold of total Fe content beyond which tetrahedral Fe first
396 appeared and then increased. If all samples are considered (below and above the total Fe threshold),
397 there is a correlation between the two variables with r^2 = 0.65 (our calculations), whereas
398 considering samples only beyond the threshold of Fe content the correlation between total and
399 tetrahedral Fe has r^2 = 0.81 (our calculations). One more study of only four samples covering a
400 large range of Fe abundance, a montmorillonite, an illite and two glauconites, provided tetrahedral
401 and total Fe contents with a very high correlation (r^2 = 0.98, our calculations) (Johnston and
402 Cardile, 1987). The assignment of Fe to tetrahedral sites is not straightforward, however the articles
403 cited above were addressing such difficulty and used careful investigations with one or several
404 complementary techniques.
405
406 All the above studies compared samples of dioctahedral composition only. The data in the present
407 study include dioctahedral (nontronite, G-N), trioctahedral (T-S) and intermediate composition (T-
408 N, Cel). A plot of total versus tetrahedral Fe of these samples revealed that the two variables are
409 correlated, although with separate correlations for each group of minerals (Figure 7). There is a

410 threshold of Fe abundance for the occurrence of tetrahedral Fe, but interestingly, this threshold is
411 different for each group of samples and increases from trioctahedral to dioctahedral compositions.
412 The results in Figure 7 show in a new light the compositional-structural control on the admittance of
413 Fe into the tetrahedral sheet of 2:1 phyllosilicates. The larger *b* crystallographic parameter of
414 trioctahedral phyllosilicates allows an almost indifferent distribution of Fe^{3+} between tetrahedral
415 and octahedral sites, whereas in dioctahedral phyllosilicates, with a smaller *b* crystallographic
416 parameter, Fe^{3+} is preferentially located in the octahedral sites (e.g., Heuser et al., 2013). These
417 results also explain the weak correlation between tetrahedral and total Fe contents when all the
418 samples are considered together, and provide the apparently fundamental reason why the color
419 parameter a^*_{10} is an ambiguous contribution towards the prediction of total Fe content. For
420 example, the approximate similar red chromaticity (produced by tetrahedral Fe content) should be
421 present in samples with similar tetrahedral Fe, but this corresponds to different total Fe contents in
422 trioctahedral and dioctahedral samples (Figure 7). The differences between mineral groups,
423 however, decrease as Fe abundance increases (Figure 7).
424
425 From the above discussion, it can be concluded that the chromatic contribution of tetrahedral Fe to
426 the prediction of total Fe content in phyllosilicates is somewhat erratic for phyllosilicates with low
427 Fe content or where trioctahedral and dioctahedral phyllosilicates are measured together. The
428 contribution, however, becomes more robust as the total amount of Fe increases. This is a plausible
429 explanation of why the CIELAB color parameters performed better in the prediction of Fe at high
430 values than at low ones (Figure 6).
431
432 Most of the investigated samples have low or no Fe^{2+} content (Table 1). No specific band that could
433 be assigned to Fe^{2+} exclusively was found. Octahedral Fe^{2+} did not correlate significantly with any
434 other Fe variable or color parameter (Table 3). For all these reasons, Fe^{2+} could not be included in

435 the regression equations to predict Fe content. Other studies of phyllosilicates with high proportion
436 of Fe^{2+} will be necessary to extend the investigation.
437
438 The use of the second derivative of the absorption spectrum to investigate Fe in Martian
439 phyllosilicates would require a simple mathematical manipulation of the spectrum. It will be
440 necessary that the spectrum has the appropriate wavelength range, resolution and signal-to-noise
441 ratio, and has been corrected for possible atmospheric modifications. There might also be need to
442 calibrate the measured amplitudes on Martian spectra to have them fit the regressions in Figure 4,
443 which could be done using amplitude ratios, rather than absolute amplitude values. The use of color
444 analysis on Mars will have similar requirements. Another second-derivative study of the visible
445 spectrum of the Martian surface is known to the authors, although of different characteristics.
446 Bishop et al. (1998) investigated the mineral composition of Martian soils in terms of Fe oxides,
447 oxy-hydroxides and oxy-hydroxysulfates, and Fe-smectites, focusing on features from 600 to 750
448 nm. Whereas this study had a different scope, it shows that this type of investigation is possible.
449
450 4.2. Framework for the investigation of Fe in Martian phyllosilicates with visible spectroscopy
451 Infrared remote sensing has revealed that phyllosilicates are present throughout the ancient Martian
452 crust (Carter et al., 2013). The position and shapes of OH and metal-OH vibrational absorptions
453 observed in the 2.18-2.4 μm wavelength range indicate that Mg-, Al-, and Fe-rich clay minerals are
454 present but that most of the deposits could be relatively Fe-rich (Michalski et al., 2015). Most of the
455 NIR data have been obtained with two instruments: the *Obervatoire pour l'Eau, la Minéralogie, les*
456 *Glaces et l'Activité* (OMEGA) and the Compact Reconnaissance Imaging Spectrometer for Mars
457 (CRISM). Both of these instruments are visible-near infrared imaging spectrometers covering an
458 approximate wavelength range of 0.45-4 μm (450-4000 nm). However, phyllosilicate analyses with
459 either instrument are generally carried out with the NIR data (1-4 μm), not using data in the visible
460 range.

NIR remote sensing on Mars allows to determine the mineralogy and octahedral composition of a wide range of phyllosilicates because the position and shape of the hydroxyl band at 2.18-2.4 μm (also, but less so, the band at ~1.4 μm) are sensitive to these two variables. However, recent investigation has pointed out that the position of the 2.18-2.4 μm band is not sensitive to compositional changes between (1) Fe-rich dioctahedral phyllosilicates and Mg-rich trioctahedral phyllosilicates with some Fe, both of which would have bands in the range 2.28-2.31 μm approximately, or (2) between trioctahedral phyllosilicates with a range of Fe-Mg substitution (Michalski et al., 2015; Cuadros et al., 2016). Color investigation of phyllosilicate deposits would be useful to assess Fe content and thus constrain the composition and nature of deposits with NIR OH bands in the indicated range. Our analyses of the visible-region spectra in the same phyllosilicate samples studied by Cuadros et al. (2016) have shown that the absorption bands at 370, 420, and 500 nm, and the CIELAB color parameters a^*_{10}, b^*_{10}, and L^*_{10} are sensitive to Fe content, in both dioctahedral and trioctahedral phyllosilicates. The visible range of the spectrum has the potential to be used complementarily with NIR in the investigation of Martian phyllosilicates.

There are, however, some complications in the use of the visible spectral range on Mars. One major issue is the fact that fine-grained silicate dust containing nanophase Fe-oxides (Morris et al., 2000) occurs throughout the planet's surface, giving it an ochre color. Some surfaces are completely blanked by dust and others contain only patchy deposits (Ruff and Christensen, 2002) but, in every case, dust needs to be considered as the possible major contributor to surface color. Spectral analyses aimed to evaluate the substrate mineralogy must be carried out with caution. In addition, the visible bands of Fe oxides and oxy-hydroxides are located closely to the important bands of octahedral Fe^{3+} bands in phyllosilicates, with the further complication that those of Fe oxides and oxy-hydroxides have greater absorptivity (Sherman and Waite, 1985; Sherman and Vergo, 1988; Scheinost et al., 1998). Further problems may be the insufficient spectral and/or spatial resolution of

487 the data coming from Mars along the entire visible region, depending on the instrument acquiring
488 the data.
489
490 Several instruments, orbiters and landers, have provided or continue acquiring visible-range
491 spectroscopic data from Mars. They typically cover the range 400-1000 nm. Spectral resolution
492 ranges from high (~7 nm for OMEGA and ~0.7 nm for CRISM) to intermediate (~50 nm for
493 instruments on rovers such as Imager for Mars Pathfinder, Pancam on Opportunity and Spirit, and
494 Mastcam on Curiosity) and low (average resolution ~130 nm for the orbiter HiRISE). Intermediate
495 to low spectral resolutions can miss features and hinder spectral analysis such as the second-
496 derivative study in this article. Instruments with intermediate to low spectral resolution, however,
497 have the advantage of their much greater spatial resolution, at the cm scale or below. In comparison,
498 OMEGA and CRISM have spatial resolutions of 300-4000 m and tens of meters, respectively. High
499 spatial resolution facilitates the investigation of surfaces free from dust, ensuring that Fe oxides and
500 oxy-hydroxides do not interfere with the investigation of phyllosilicates.
501
502 HiRISE data have been used before to extend clay mineralogy observed in CRISM data to much
503 higher spatial resolution using color differences (Bennett et al., 2012). For example, the Mawrth
504 Vallis region of Mars contains Al-rich clays and Fe^{3+}-rich clays (Bishop et al., 2008b). In a
505 particular location (Figure 8a), CRISM NIR data clearly show vibrational OH and metal-OH
506 absorptions indicative of the different clay minerals (bands at 2200 nm for Al-rich, at 2300 nm for
507 Fe-rich; Figure 8c). The corresponding CRISM visible data of the same surfaces are mostly
508 featureless, but they do show differences in slope related to mineralogy (Figure 8b). The visible
509 spectrum of Al-rich clays had higher reflectance in the blue-green wavelengths and lower in the red
510 ones than the Fe-rich clays. This relationship is made clearer using HiRISE data (Figure 8d), which
511 show the blueish hue of the Fe-poor (Al-rich) clays and reddish hue of the Fe-rich clays.
512

HiRISE data calibrated to I/F (similar to reflectance) of other well studied phyllosilicate deposits showed additional diversity (Figure 9). Here, there is much higher spatial resolution (0.25 m/pixel) than in the CRISM data (tens of meters per pixel), but the spectral resolution is lower with only three channels (on average: 500 nm, 700 nm, and 900 nm). The two spectra from Mawrth Vallis follow the same pattern in relation to Al-Fe composition as in Figure 8. The formation of Fe/Mg- and Al-phyllosilicates in Mawrth Vallis has been proposed to be caused by processes ranging from underground hydrothermal alteration (especially Fe/Mg-clay) to supergene alteration of basalt or previous clay (especially Al-clay) (Ehlmann et al., 2011; Michalski et al., 2013; Carter et al., 2013). Phyllosilicates in the Eridania basin, which are interpreted to have formed in a hydrothermal seafloor environment (Michalski et al., 2017), have lower overall reflectance in HiRISE data than phyllosilicates from the Mawrth Vallis. This fact may be due to the presence of tetrahedral Fe in the Eridania phyllosilicates and its absence in those of Mawrth Vallis, as such appeared to be an important control of spectrum reflectance in our samples (compare Nontronite 33B and Nontronite 51 with the other samples, Table 1, Figure 1). The Eridania materials are high in Fe and Mg (Michalski et al., 2017), and would be comparable to our submarine hydrothermal T-N, G-N and Fe-rich T-N. The Nili Fossae phyllosilicates containing Fe and/or Mg (Mangold et al., 2007), which are also likely of hydrothermal origin (Ehlmann et al., 2009), have even lower overall reflectance, which might indicate a higher total tetrahedral and total Fe content than in Eridania. Indeed, a combination of mid-infrared and NIR analyses concluded that the Nili Fossae clays could be extremely Fe-rich (Michalski et al., 2010).

In summary, although with low spatial resolution (CRISM data) and only at crude spectral resolution (HiRISE data), these few examples of spectral curves from Mars phyllosilicates appear comparable to our spectral dataset of phyllosilicates from Earth (Figure 1). The Martian spectra show a variability of spectral characteristics in the visible range that may be linked to Fe content and structural sites in the phyllosilicates and to the specific environment where they formed, as do

539 the Earth samples from our study. These findings are encouraging to test spectral and color analysis
540 on Martian rocks. The laboratory analyses in the visible range presented here could potentially
541 apply to spectra from Martian phyllosilicates to assess their Fe content. The main current problems
542 for this application are the following. There is not the same coverage at the short wavelength of the
543 spectrum in Mars data (most frequently starting at 400 nm, although CRISM covers from 362 nm)
544 as there is in laboratory studies, meaning that some of the indices employed in this article may not
545 be calculated. The spectral resolution of most of the various Mars datasets are coarser than those
546 from the laboratory, so that application of the parameters from this study might require some
547 calibration or modification. In addition, the studies will require ascertaining that the investigated
548 rocks are sufficiently free from Fe oxides and oxy-hydroxides, as well as from other interfering
549 phases. This latter task is easily performed in investigations carried out with data from landers,
550 given the proximity and size of the targets, and it is also feasible in data from orbiters where it is
551 possible to combine results from several complementary techniques.
552
553 **5. Conclusions**
554 Spectral data in the visible region have shown to be useful for identifying quantitatively the
555 presence of Fe^{3+} in simple end-members and complex mixtures of end-member and interstratified
556 phyllosilicates with a wide range of Fe content and including dioctahedral, trioctahedral, and
557 intermediate dioctahedral-trioctahedral compositions. Two approaches were used, one based on the
558 amplitudes of certain bands in the second derivative of the Kubelka-Munk spectrum, the other
559 based on the calculation of CIELAB color parameters from the reflectance spectrum. The color-
560 parameter approach produced marginally better results and was more universally applicable than the
561 second-derivative approach. It was also possible to detect the existence of Fe^{3+} in octahedral and
562 tetrahedral positions with both methods. Octahedral Fe^{3+} was manifested by a 370 nm band and
563 yellow chromaticity indicated by the CIELAB parameter b^*_{10}. Tetrahedral Fe^{3+} was revealed by a
564 band at 420 nm and red chromaticity indicated by the CIELAB parameter a^*_{10}. However, the

565 contribution of red chromaticity to the prediction of total Fe content is complicated by the fact that
566 phyllosilicates of dioctahedral and trioctahedral composition have different behavior in the
567 distribution of Fe^{3+} between tetrahedral and octahedral sites (e.g, similar red chromaticity, or
568 tetrahedral Fe content, correspond with different total Fe content in dioctahedral and trioctahedral
569 compositions). The color parameter lightness (L^*_{10}) is inversely related with Fe^{3+}, regardless of its
570 structural position. Many of the samples contained little or no Fe^{2+} and this precluded finding
571 parameters or bands identifying Fe^{2+}.
572
573 A few Mars spectra selected from areas where Fe-rich phyllosilicates exist provide a spectral
574 variety similar to that found in the investigated phyllosilicates from Earth. Full test of the
575 applicability of the results from this study to the investigation of Fe on Mars will require
576 appropriate wavelength coverage and spectral resolution from Mars datasets, as well as guarantee of
577 lack of interference from the widespread Fe oxides. However, the variability of the Martian visible
578 spectra examined here is encouraging to follow this line of investigation.
579
580 **Acknowledgements**
581 This work was supported by the European Commission (Hydro-Mars project) and the Ministry of
582 Economy and Competitiveness of the National Government of Spain (research project FIS2016-
583 80983-P) with assistance from European Regional Development Fund (ERDF).
584

585 **References**

586

587 Baumgardner, M.F., Silva, L.F., Biehl, L.L., Stoner, R., 1985. Reflectance properties of soils. Adv.
588 Agron. 38, 1-44.

589

590 Bennett, K.A., Bell III, J.F., McConnochie, T.H., Wolff, M.J., 2012. Extendeing CRISM spectral
591 coverage in Gale Crater using THEMIS-VIS and HiRISE. 43rd Lunar and Planetary Science
592 Conference, abstract 2761.

593

594 Bishop, J., Pieters, C., Edwards, J., 1994, Infrared spectroscopic analyses on the nature of water in
595 montmorillonite. Clay Clay Miner. 42, 702-716.

596

597 Bishop, J.L., Murad, E., 1996. Schwertmannite on Mars? Spectroscopic analyses of
598 schwertmannite, its relationship to other ferric minerals, and its possible presence in the surface
599 material on Mars. In: Dyar, M.D., et al. (Eds.), Mineral Spectroscopy: A Tribute to Roger G. Burns
600 Spec. Pub. 5. The Geochemical Society, St Louis, MO, pp. 337–358.

601

602 Bishop, J.L., Scheinost, A., Bell, III, J.F., Britt, D., Johnson, J.R., Murchie, S., 1998. Ferrihydrite-
603 Schwertmannite-silicate mixtures as a model of martian soils measured by Pathfinder. 29th Lunar
604 and Planetary Science Conference, abstract 1803.

605

606 Bishop, J., Lane, M., Dyar, M.D., Brown, A., 2008a. Reflectance and emission spectroscopy study
607 of four groups of phyllosilicates: smectites, kaolinite-serpentines, chlorites and micas. Clay Miner.
608 43, 35-54.

609

610 Bishop, J.L., Noe Dobrea, E.Z., McKeown, N.K., Parente, M., Ehlmann, B.L., Michalski, J.R.,
611 Milliken, R.E., Poulet, F., Swayze, G.A., Mustard, J.F., Murchie, S.L., Bibring, J.-P., 2008b.
612 Phyllosilicate diversity and past aqueous activity revealed at Mawrth Vallis, Mars. Science 321,
613 830-833. DOI: 10.1126/science.1159699
614
615 Blewett, D.T., Hawke, B.R., Lucey, P.G., Taylor, G.J., Jaumann, R., Spudis, P.D., 1995. Remote
616 sensing and geologic studies of the Schiller-Schickard region of the Moon. J. Geophys. Res. Planets
617 100, 16959-16977. DOI: 10.1029/95JE01409
618
619 Bouzidi, N., Siham, A., Concha-Lozano, N., Gaudon, P., Janin, G., Mahtout, L., Merabet, D., 2014.
620 Effect of chemico-mineralogical composition on color of natural and calcined kaolins. Color Res.
621 and Appl. 39, 499-505.
622
623 Burns, R.G., 1993. Mineralogical Applications of Crystal Field Theory. 2nd ed. Cambridge
624 University Press, Cambridge.
625
626 Carter J., Poulet F., Bibring J.-P., Mangold N., Murchie S., 2013. Hydrous minerals on Mars as
627 seen by the CRISM and OMEGA imaging spectrometers: Updated global view. J. Geophys. Res.
628 Planets 118, 831-858.
629
630 CIE, 2004. Publication 15:2004. In: Bureau, C.C. (Ed.), Colorimetry, 3rd ed. (Vienna).
631
632 Cuadros, J., Michalski, J.R., 2013. Investigation of Al-rich clays on Mars: evidence for kaolinite-
633 smectite mixed-layer versus mixture of end-member phases. Icarus 222, 296-306. doi
634 http://dx.doi.org/10.1016/j.icarus.2012.11.006
635

636 Cuadros, J., Michalski, J.R., Dekov, V., Bishop, J., Fiore, S., Dyar, M.D., 2013. Crystal-chemistry
637 of interstratified Mg/Fe-clay minerals from seafloor hydrothermal sites. Chem. Geol. 360-361, 142-
638 158. DOI: http://dx.doi.org/10.1016/j.chemgeo.2013.10.016
639
640 Cuadros, J., Michalski, J.R., Dekov, V., Bishop, J.L., 2016. Octahedral chemistry of 2:1 clay
641 minerals and hydroxyl band position in the near-infrared. Application to Mars. Am. Mineral. 101,
642 554-563.DOI: http://dx.doi.org/10.2138/am-2016-5366
643
644 Ehlmann, B.L., Mustard, J.F., Swayze, G.A., Clark, R.N., Bishop, J.L., Poulet, F., Des Marais, D.J.,
645 Roach, L.H., Milliken, R.E., Wray, J.J., Barnouin-Jha, O., Murchie, S.L., 2009. Identification of
646 hydrated silicate minerals on Mars using MRO-CRISM: Geologic context near Nili Fossae and
647 implications for aqueous alteration. J. Geophys. Res. Planets 114,
648 https://doi.org/10.1029/2009JE003339
649
650 Ehlmann, B.L., Mustard, J.F., Murchie, S.L., Bibring, J.P., Meunier, A., Fraeman, A.A., Langevin,
651 Y., 2011, Subsurface water and clay mineral formation during early history of Mars. Nature 479,
652 53-60.
653
654 Fan, C., Xie, H., Wu, J., Birnbaum, S., 2012. Analysis of United States Geological Survey spectral
655 library of silicate minerals: implication forremote sensing applications. J. Appl. Remote Sens. 6,
656 063514.
657
658 Farrand, W.H., Bell III J.F., Johnson, J.R., Bishop, J.L., Morris, R.V., 2008. Multispectral imaging
659 from Mars Pathfinder. The Martian Surface: Composition, Mineralogy, and Physical Properties. J.
660 F. Bell III (ed). Cambridge University Press. 265-280.
661

662 Gámiz, E., Melgosa, M., Sánchez-Marañón, M., Martín García, J.M., Delgado R., 2005.
663 Relationships between chemico-mineralogical composition and color properties in selected natural
664 and calcined Spanish kaolins. Appl. Clay Sci. 28, 269-282.
665
666 Gámiz, E., Párraga, J., Sánchez-Marañón, M., Melgosa, M., Fernández-González, M.V., Delgado
667 R., 2011. Is the pharmacopoeia test a good estimator of the organic impurities in Kaolin? Appl.
668 Clay Sci. 51, 431-437.
669
670 Gates, W.P., Slade, P.G., Manceau, A., Landon, B., 2002. Site occupancies by iron in nontronites.
671 Clays Clay Miner. 50, 223-239.
672
673 Heuser, M., Andrieux, P., Petit, S., Stanjek, H., 2013. Iron-bearing smectites: a revised relationship
674 between structural Fe, *b* cell edge lengths and refractive indices. Clay Miner. 48, 97-103. DOI:
675 https://doi.org/10.1180/claymin.2013.048.4.06
676
677 Johnston, J.H., Cardile, C.M., 1987. Iron substitution in montmorillonite, illite and glauconite by
678 ^{57}Fe Mössbauer spectroscopy. Clays Clay Miner. 35, 170-176.
679
680 Kaufhold, S., Stucki, J.W., Finck, N., Steininger, R., Zimina, A., Dohrmann, R., Ufer, K., Pentrák,
681 M., Pentráková, L., 2017. Tetrahedral charge and Fe content in dioctahedral smectites. Clay Miner.
682 52, 51-65. DOI: https://doi.org/10.1180/claymin.2017.052.1.03
683
684 Lear, P.R., Stucki, J.W., 1987. Intervalence electron transfer and magnetic exchange in reduced
685 nontronite. Clays Clay Miner. 35, 373-378.
686

McKeown, N.K., Bishop, J.L., Cuadros, J., Hillier, S., Amador, E., Makarewicz, H.D., Parente, M., Silver, E.A., 2011. Interpretation of reflectance spectra of clay mineral-silica mixtures: implications for Martian clay mineralogy at Mawrth Vallis. Clays Clay Miner. 59, 400-415. doi 10.1346/CCMN.2011.0590404

Mangold, N., Poulet, F., Mustard, J.F., Bibring, J.-P., Gondet, B., Langevin, Y., Ansan, V., Masson, Ph., Fassett, C., Head, J.W. III, Hoffmann, H., Neukum, G., 2007. Mineralogy of the Nili Fossae region with OMEGA/Mars Express data: 2. Aqueous alteration of the crust. J. Geophys. Res. Planets 112, E8, https://doi.org/10.1029/2006JE002835

Michalski, J., Poulet, F., Bibring, J.P., Mangold, N., 2010. Analysis of phyllosilicate deposits in the Nili Fossae region of Mars: Comparison of TES and OMEGA data. Icarus 206, 269–289.

Michalski, J.R., Niles, P.B., Cuadros, J., Balbridge, A.M., 2013. Multiple working hypotheses for the formation of compositional stratigraphy on Mars: Insights from the Mawrth Vallis region. Icarus 226, 816-840. doi http://dx.doi.org/10.1016/j.icarus.2013.05.024

Michalski, J.R., Cuadros, J., Bishop, J.L., Dyar, M.D., Dekov, V., Fiore, S., 2015. Constraints on the crystal-chemistry of Fe/Mg-rich smectitic clays on Mars and links to global alteration trends. Earth Planet. Sci. Lett. 427, 215-225. doi:10.1016/j.epsl.2015.06.020

Michalski, J.R., Noe Dobrea, E.Z., Niles, P.B., Cuadros, J., 2017. Ancient hydrothermal seafloor deposits in Eridania basin on Mars. Nat. Commun. 8:15978. DOI: http://www.nature.com/articles/ncomms15978

712 Milliken, R.E., Bish, D.L., Bristow, T., Mustard, J.F., 2010. The case for mixed-layered clays on
713 Mars. Lunar and Planetary Science Conference, 41, 2030.
714
715 Moroz, L., Schade, U., Wäsch, R., 2000. Reflectance spectra of olivine–orthopyroxene-bearing
716 assemblages at decreased temperatures: Implications for remote sensing of asteroids. Icarus, 147,
717 79-93. https://doi.org/10.1006/icar.2000.6430
718
719 Morris, R.V., Golden, D.C., Bell III, J.F., Shelfer, T.D., Scheinost, A.C., Hinman, N.W., Furniss,
720 G., Mertzman, S.A., Bishop, J.L., Ming, D.W., Allen, C.C., Britt, D.T., 2000. Mineralogy,
721 composition, and alteration of Mars Pathfinder rocks and soils: Evidence from multispectral,
722 elemental, and magnetic data on terrestrial analogue, SNC meteorite, and Pathfinder samples. J.
723 Geophys. Res. Planets, 105, 1757-1817.
724
725 Mussel, W.N., Murad, E., Criscuolo, P.S.R., Pinheiro, P.G., Fabris, J.D., 2008. Variation in
726 mineralogy during the beneficiation of Capim Kaolin from Pará Brazil. Clay Min. 43, 381-391.
727
728 Ruff, S.W., Christensen, P.R., 2002. Bright and dark regions on Mars: Particle size and
729 mineralogical characteristics based on Thermal Emission Spectrometer data. J. Geophys. Res. 107,
730 E12, 5127, doi:10.1029/2001JE001580.
731
732 Sánchez-Marañón, M., García, P.A., Huertas, R., Hernández-Andrés, J., Melgosa, M., 2011.
733 Influence of natural daylight on soil color description: assessment using a color-appearance model
734 Soil Sci. Soc. Am. J. 75, 984-993.
735
736 Sánchez-Marañón, M., Romero-Freire, A., Martín-Peinado, F.J., 2015. Soil-color changes by
737 sulfuricization induced from a pyritic surface sediment. Catena 135, 173–183.

Sánchez-Marañón, M., Soriano M., Melgosa M., Delgado G., Delgado, R., 2004. Quantifying the effects of aggregation, particle-size and components on the colour of Mediterranean soils. Eur. J. Soil Sci. 55, 551-565.

Savitzky, A., Golay, M.J.E., 1964. Smoothing and differentiation of data by simplified least squares procedures. Anal. Chem. 36, 1627-1639.

Schabenberger, O., Pierce, F.J., 2002. Contemporary Statistical Models for Plant and Soil Sciences. CRC Press, Washington, DC.

Schäfer,T., Nathues, A., Mengel, K., Izawa, M.R.M., Cloutis, E.A., Schäfer, M., Hoffmann, M., 2016. Spectral parameters for Dawn FC color data: Carbonaceous chondrites and aqueous alteration products as potential cerean analog materials. Icarus 265, 149-160.

Scheinost, A.C., Schwertmann, U., 1999. Color identification of iron oxides and hydroxysulfates: use and limitations. Soil Sci. Soc. Am. J. 63, 1463–1471.

Scheinost, A.C., Chavernas, A., Barrón, V., Torrent, J., 1998. Use and limitations of the second-derivative diffuse reflectance spectroscopy in the visible to near-infrared range to identify and quantify Fe oxide minerals in soils. Clay Clay Miner. 46, 528–536.

Sellitto, V.M., Fernandes, R.B.A., Barrón, V., Colomo, C., 2009. Comparing two different spectroscopic techniques for the characterization of soil iron oxides: Diffuse versus bi-directional reflectance. Geoderma 149, 2-9.

764 Sherman, D.M., Vergo, N., 1988. Optical (diffuse reflectance) and Mössbauer spectroscopic study
765 of nontronite and related Fe-bearing smectites. Am. Mineral. 73, 1346-1354.
766
767 Sherman, D.M., Waite, T.D., 1985. Electronic spectra of Fe3+ oxides and oxide hydroxides in the
768 near IR to near UV. Am. Mineral. 70, 1262–1269.
769
770 Soriano, M., Melgosa, M., Sánchez-Marañón, M., Delgado, G., Gámiz, E., Delgado, R., 1998.
771 Whiteness of talcum powders as a quality index for pharmaceutical uses. Color Res. Appl. 23, 178-
772 185.
773
774 Soriano, M., Sánchez-Marañón, M., Melgosa, M., Gámiz, E, Delgado, R., 2002. Influence of
775 chemical and mineralogical composition on color for commercial talcs. Color Res. Appl. 27, 430-
776 440.
777
778 Torrent, J., Barrón, V., 2002. Diffuse reflectance spectroscopy of iron oxides. Encyclopedia of
779 Surface and Colloid Science. Marcel Dekker, Inc. 1438-1446.

Table 1. Mineralogy and chemical formulas of the phyllosilicate samples calculated on the basis of $O_{10}(OH)_2$ (Cuadros et al., 2013).

Sample	Min	% DiSmec	% TriSmec	Si	Al tet	Fe tet	Al oct	Mg oct	Fe III	Fe II	Mn	Ti	Mg intl	Ca	Na	K	Sum oct
Va22-146KS (1144-1145)	G-N	68		3.93	0.05	0.02	0.00	0.25	1.69	0.05	0.00	0.00	0.00	0.00	0.12	0.25	2.00
Va22-146KS(612-614)	G-N	59		3.68	0.09	0.23	0.02	0.20	1.79	0.00	0.00	0.00	0.00	0.09	0.00	0.27	2.02
Va22-146KS(588-591)	G-N	56		3.73	0.00	0.27	0.05	0.17	1.73	0.04	0.00	0.00	0.00	0.09	0.00	0.35	1.99
Va22-146KS(603-604)	G-N	50		3.74	0.04	0.22	0.03	0.18	1.79	0.00	0.00	0.00	0.00	0.06	0.00	0.33	2.00
Va22-146KS(1145-1146)	G-N	47		3.95	0.05	0.00	0.04	0.25	1.65	0.05	0.00	0.00	0.00	0.01	0.11	0.24	1.99
Va22-146KS(586-587)	G-N	39		3.55	0.09	0.36	0.02	0.18	1.83	0.04	0.00	0.00	0.00	0.07	0.00	0.30	2.08
Va22-146KS(639-640)	G-N	33		3.62	0.00	0.38	0.00	0.23	1.84	0.00	0.00	0.00	0.00	0.05	0.00	0.28	2.08
Va22-146KS(1030-1034)	G-N	23		3.80	0.02	0.18	0.06	0.17	1.58	0.11	0.05	0.00	0.00	0.04	0.03	0.49	1.98
Glauconite 97	G-N	4		3.45	0.55	0.00	0.33	0.15	1.33	0.19	0.00	0.01	0.10	0.02	0.02	0.63	2.00
1183-15	N	100		3.62	0.01	0.37	0.00	0.31	1.67	0.00	0.01	0.00	0.00	0.00	0.40	0.31	1.99
Cy 82-14-5	N	100		3.60	0.04	0.36	0.00	0.28	1.76	0.00	0.00	0.00	0.00	0.03	0.48	0.03	2.04
Nontronite 33B	N	100		3.54	0.46	0.00	0.09	0.03	1.88	0.00	0.00	0.00	0.01	0.23	0.00	0.00	2.00
Va3-413KH (150-153)	T-N	80		3.11	0.23	0.66	0.00	0.55	1.68	0.07	0.02	0.00	0.00	0.13	0.16	0.13	2.33
Nontronite 51	T-N	76		3.92	0.08	0.00	0.00	0.82	1.09	0.15	0.00	0.01	0.00	0.20	0.01	0.40	2.08
Va22-146KS(471-475)	T-N	75		3.24	0.14	0.62	0.14	0.15	1.69	0.20	0.01	0.01	0.00	0.10	0.09	0.21	2.21
Va22-146KS(575-577)	T-N	71		3.40	0.10	0.50	0.03	0.18	1.92	0.00	0.00	0.00	0.00	0.12	0.00	0.15	2.13
Va22-146KS(583-586)	T-N	69		3.42	0.21	0.37	0.05	0.18	1.96	0.00	0.00	0.01	0.00	0.00	0.01	0.13	2.21
CHN-100-18PC (290-292)	T-N	68		3.13	0.37	0.50	0.00	0.18	1.81	0.20	0.08	0.01	0.00	0.19	0.00	0.09	2.28
Va22-146KS(602-603)	T-N	60		3.13	0.45	0.42	0.00	0.28	1.97	0.00	0.01	0.01	0.00	0.09	0.03	0.11	2.27
CRB 03-026	Cel, Sap		25	3.65	0.31	0.04	0.00	0.90	1.00	0.23	0.01	0.07	0.10	0.00	0.07	0.55	2.20
Va3-413KH (382-389)	T-S		90	3.59	0.21	0.20	0.00	2.03	0.51	0.18	0.00	0.01	0.00	0.06	0.31	0.00	2.73
Va1-52KH (323-327)	T-S		67	3.77	0.23	0.00	0.01	2.81	0.18	0.00	0.00	0.01	0.00	0.00	0.02	0.00	3.00
Sea Cliff Dive 308	T-S		27	3.86	0.05	0.09	0.06	2.58	0.05	0.29	0.00	0.00	0.00	0.01	0.02	0.01	2.99
POS-291-459 SL (155-158)	T-S		27	3.82	0.18		0.00	2.95	0.03	0.03	0.00	0.00	0.00	0.03	0.04	0.01	3.01
M64/1 139GTV-5E (Turtle Pits)	T-S		21	3.78	0.19	0.03	0.00	2.80	0.03	0.20	0.00	0.00	0.00	0.00	0.13	0.00	3.03
POS-291-459 SL(56-57)	T-S		20	3.82	0.18		0.00	2.82	0.07	0.05	0.00	0.01	0.00	0.05	0.07	0.01	2.96
Va3-413KH (313-318)	T-S		18	3.76	0.06	0.18	0.00	2.51	0.24	0.20	0.00	0.00	0.00	0.05	0.00	0.00	2.94
POS-291-459 SL(31-32)	T-S		17	3.87	0.13		0.00	2.94	0.04	0.02	0.00	0.00	0.00	0.01	0.05	0.01	3.00
POS-291-459 SL(140-141)	T-S		16	3.86	0.14		0.00	2.96	0.03	0.02	0.00	0.00	0.00	0.01	0.05	0.01	3.01
POS-291-459 SL(113-114)	T-S		13	3.87	0.13		0.00	2.95	0.03	0.02	0.00	0.00	0.00	0.01	0.04	0.01	3.00
St. 631 6 (Logatchev-2)	T-S		11	3.96	0.04		0.00	2.78	0.10	0.00	0.01	0.00	0.00	0.01	0.02	0.01	2.90
POS-291-459 SL(20-21)	T-S		10	3.88	0.11		0.00	2.92	0.03	0.02	0.00	0.00	0.00	0.02	0.06	0.01	2.98
POS-291-459 SL(72-73)	T-S		6	3.84	0.16		0.00	3.01	0.01	0.01	0.00	0.00	0.00	0.01	0.04	0.01	3.04
1183-9	T-S		2	3.57	0.04	0.39	0.00	1.52	0.75	0.55	0.01	0.00	0.00	0.01	0.00	0.00	2.83

Cel: celadonite; G-N: interstratified glauconite-nontronite; N: nontronite; Sap: saponite; T-N: interstratified talc-nontronite; T-S: interstratified talc-saponite.

DiSmec: dioctahedral smectite (nontronite); TriSmec: trioctahedral smectite (saponite).

Table 2. CIELAB color parameters of the studied samples.

Sample	L^*_{10}	a^*_{10}	b^*_{10}	$C^*_{ab,10}$	$h_{ab,10}$
Va22-146KS (1144-1145)	38.43	-2.12	14.31	14.46	98.43
Va22-146KS (612-614)	36.31	3.28	19.51	19.78	80.45
Va22-146KS (588-591)	38.37	2.02	19.98	20.08	84.23
Va22-146KS (603-604)	38.79	2.23	20.89	21.01	83.91
Va22-146KS (1145-1146)	38.31	0.03	17.48	17.48	89.90
Va22-146KS (586-587)	44.35	5.89	27.70	28.32	77.99
Va22-146KS (639-640)	47.11	3.68	26.30	26.55	82.03
Va22-146KS (1030-1034)	39.41	0.34	18.87	18.87	88.98
Glauconite 97	43.35	-4.66	11.82	12.71	111.52
1183-15	40.98	2.60	23.95	24.09	83.80
Cy 82-14-5	38.64	5.96	20.65	21.49	73.91
Nontronite 33B	76.63	-2.15	32.16	32.23	93.82
Va3-413KH (150-153)	29.27	3.49	13.88	14.31	75.89
Nontronite 51	85.84	-6.18	32.71	33.29	100.70
Va22-146KS (471-475)	38.29	10.90	26.55	28.70	67.67
Va22-146KS (575-577)	38.39	12.61	26.48	29.33	64.53
Va22-146KS (583-586)	41.43	12.79	30.17	32.77	67.03
CHN-100-18PC (290-292)	33.13	7.67	20.38	21.77	69.36
Va22-146KS (602-603)	35.68	11.08	23.92	26.37	65.14
CRB 03-026	40.44	3.93	11.28	11.94	70.78
Va3-413KH (382-389)	33.99	2.83	10.83	11.19	75.34
Va1-52KH (323-327)	63.49	2.40	10.70	10.97	77.37
Sea Cliff Dive 308	67.94	-0.64	15.48	15.49	92.35
POS-291-459 SL (155-158)	67.20	2.22	11.79	11.99	79.32
M64/1 139GTV-5E (Turtle Pits)	66.39	-2.97	4.37	5.28	124.15
POS-291-459 SL (56-57)	49.69	1.00	11.11	11.15	84.87
Va3-413KH (313-318)	54.47	12.33	18.70	22.40	56.59
POS-291-459 SL (31-32)	70.97	0.86	14.61	14.63	86.65
POS-291-459 SL (140-141)	71.94	2.29	11.30	11.53	78.53
POS-291-459 SL (113-114)	68.21	2.42	9.70	10.00	76.02
St. 631 6 (Logatchev-2)	78.32	0.61	16.36	16.37	87.87
POS-291-459 SL (20-21)	77.06	0.55	12.54	12.55	87.47
POS-291-459 SL (72-73)	63.32	2.73	9.02	9.43	73.15
1183-9	47.16	8.40	20.39	22.05	67.62

Table 3. Significant correlation coefficients at $P < 0.05$ ($n = 34$) between CIELAB color parameters and Fe content.

	a^*_{10}	b^*_{10}	$C^*_{ab,10}$	$h_{ab,10}$	Tet Fe^{3+}	Oct Fe^{3+}	Oct Fe^{2+}	Total Fe
L^*_{10}	-0.4663			0.3552	-0.6811	-0.6896		-0.7460
a^*_{10}			0.4177	-0.8736	0.6947			0.4040
b^*_{10}			0.9930		0.4955	0.7085		0.6988
$C^*_{ab,10}$					0.5349	0.6998		0.7046
$h_{ab,10}$					-0.5313			
Tet Fe^{3+}						0.6446		0.7833
Oct Fe^{3+}								0.9714
Oct Fe^{2+}								

Tet: Tetrahedral
Oct: Octahedral

Figure captions

Figure 1. Reflectance spectra of the investigated samples, arranged according to their mineralogy and from dioctahedral composition (a] nontronite, b] glauconite-nontronite) to samples with intermediate dioctahedral-trioctahedral composition (c] talc-nontronite and CRB 03-26, a mixture of celadonite and saponite), and to trioctahedral composition (d] talc-saponite). The samples are from seafloor hydrothermal sites, except Nontronite 33B in a), Glauconite 97 in b), and Nontronite 51and CRB 03-026 in c), which have a continental origin.

Figure 2. Second derivative of the Kubelka-Munk spectra of the samples. The spectra are grouped and their color is coded as in Figure 1. The arrows at the minima indicate the wavelength, or range of wavelength, where the absorption bands are located.

Figure 3. Several Fe content variables regressed on the amplitude of absorption bands in the second-derivative Kubelka-Munk spectra. The amplitude corresponds to the absorption bands centered at 370 nm ($A_{370\text{-}400}$), 420 nm ($A_{420\text{-}450}$), and 500 nm ($A_{500\text{-}560}$). The Fe contents measured in the phyllosilicates, as atoms per half formula unit, are: Fe^{3+} in the octahedral sheets, Fe^{3+} in the tetrahedral sheets, total Fe^{3+} content, and total Fe content. Samples Nontronite 33B and Nontronite 51, of continental origin, were not used in this analysis (see text).

Figure 4. Plot of observed versus predicted values of (a) the total Fe content (atoms per half formula unit) and (b) the Fe/(Fe+Mg+Al) ratio in each sample. The predictive multiple linear-regression model used the amplitudes of the absorption bands at 370 nm ($A_{370\text{-}400}$) and 420 nm ($A_{420\text{-}450}$) in the second-derivative Kubelka-Munk spectra.

Figure 5. Casement scatter plot of CIELAB chromatic coordinates (a^*_{10} and b^*_{10}) by L^*_{10} levels. This plot represents three variables in two dimensions. Each L^*_{10} level depicts a casement, in which a^*_{10} and b^*_{10} are the x- and y-variables. The range of a^*_{10} and b^*_{10} values in each casement is -7 to 13 and 0 to 40, respectively.

Figure 6. Plot of observed versus predicted values of (a) the total Fe content (atoms per half formula unit) and (b) the Fe/(Fe+Mg+Al) ratio in each sample. The predictive multiple linear-regression model used the CIELAB color parameters L^*_{10}, a^*_{10}, and b^*_{10} as independent variables.

Figure 7. Correlations between total and tetrahedral Fe (Table 1) for each individual group of samples: nontronite, galuconite-nontronite (G-N), talc-nontronite (T-N) and talc-saponite (T-S). No correlation line was added for nontronite as there are only 3 data points. There is a threshold of total Fe content for the occurrence of tetrahedral Fe, and this threshold increases from trioctahedral (T-S) to intermediate (T-N) and to dioctahedral (N and G-N) composition.

Figure 8. Images and spectra of the Mawrth Vallis region of Mars. CRISM data of phyllosilicate-rich horizons in bedrock exposed in the wall of a crater (a), as well as their spectra in the visible (b) and NIR (c) range. A 3-D view of HiRISE color data draped onto HiRISE topography data (d) shows the color difference between Al-clays and Fe/Mg-clays in IRB (infrared, red and blue-green wavelengths assigned to RGB in the image).

Figure 9. Images and visible spectra from HiRISE IRB (infrared, red and blue-green wavelengths assigned to RGB in the image) data of three areas of Mars with abundant phyllosilicates: Mawrth Vallis, Nili Fossae, and Eridania basin. The red spectrum in Marwth Vallis corresponds to the box in the yellowish terrain (top of the image); the blue spectrum, to the bluish terrain (left of the image). Views are ~1 km across. The spectral data are calibrated to I/F (similar to reflectance), but

the display hues are not quantitatively cross-calibrated. Even so, their spectra show differences in reflectance.

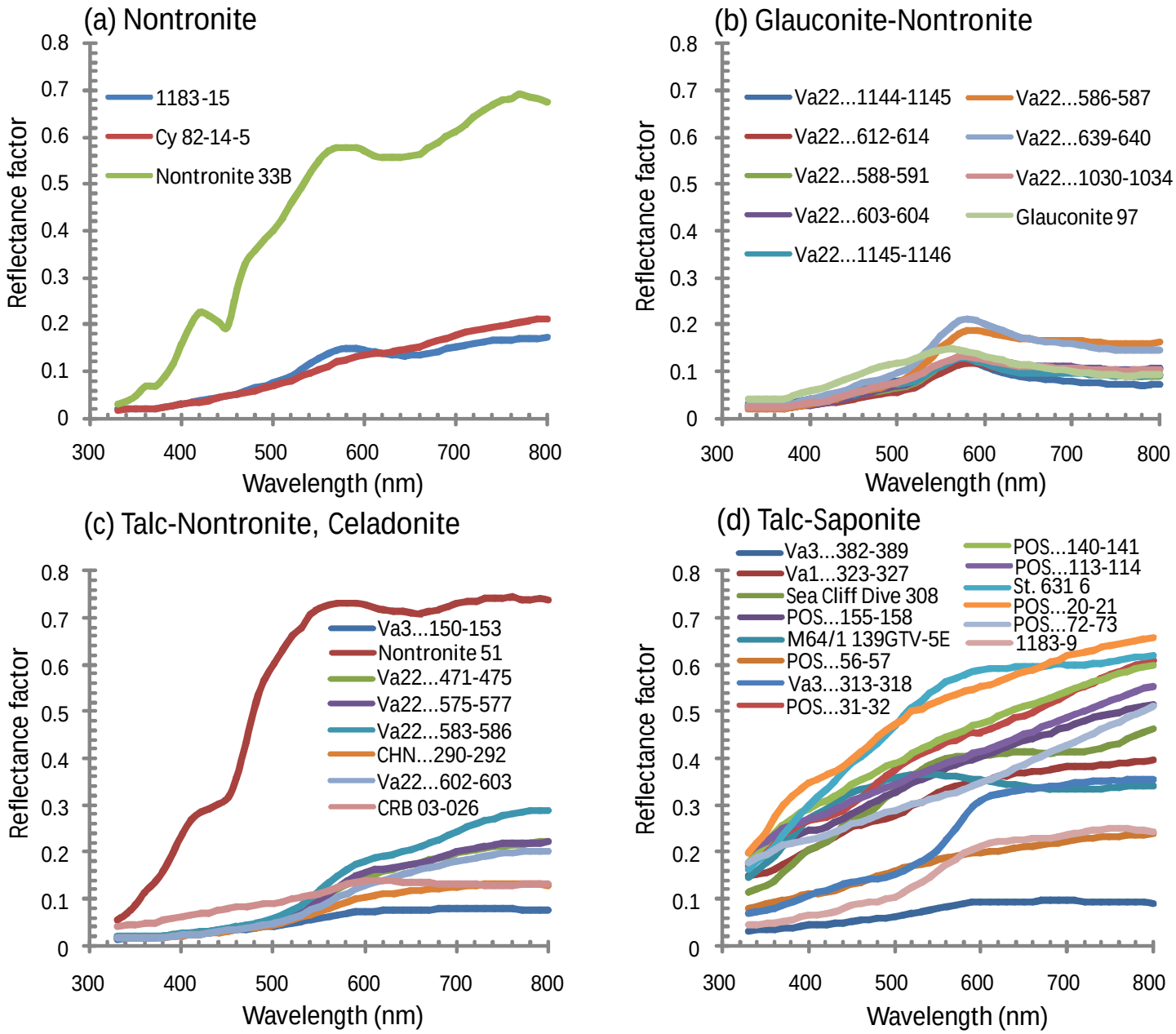
(a) Nontronite
Reflectance factor
Wavelength (nm)
1183-15
Cy 82-14-5
Nontronite 33B
(b) Glauconite-Nontronite
Va22...1144-1145
Va22...586-587
Va22...612-614
Va22...639-640
Va22...588-591
Va22...1030-1034
Va22...603-604
Glauconite 97
Va22...1145-1146
(c) Talc-Nontronite, Celadonite
Va3...150-153
Nontronite 51
Va22...471-475
Va22...575-577
Va22...583-586
CHN...290-292
Va22...602-603
CRB 03-026
(d) Talc-Saponite
Va3...382-389
Va1...323-327
Sea Cliff Dive 308
POS...155-158
M64/1 139GTV-5E
POS...56-57
Va3...313-318
POS...31-32
POS...140-141
POS...113-114
St. 631 6
POS...20-21
POS...72-73
1183-9

Figure 1

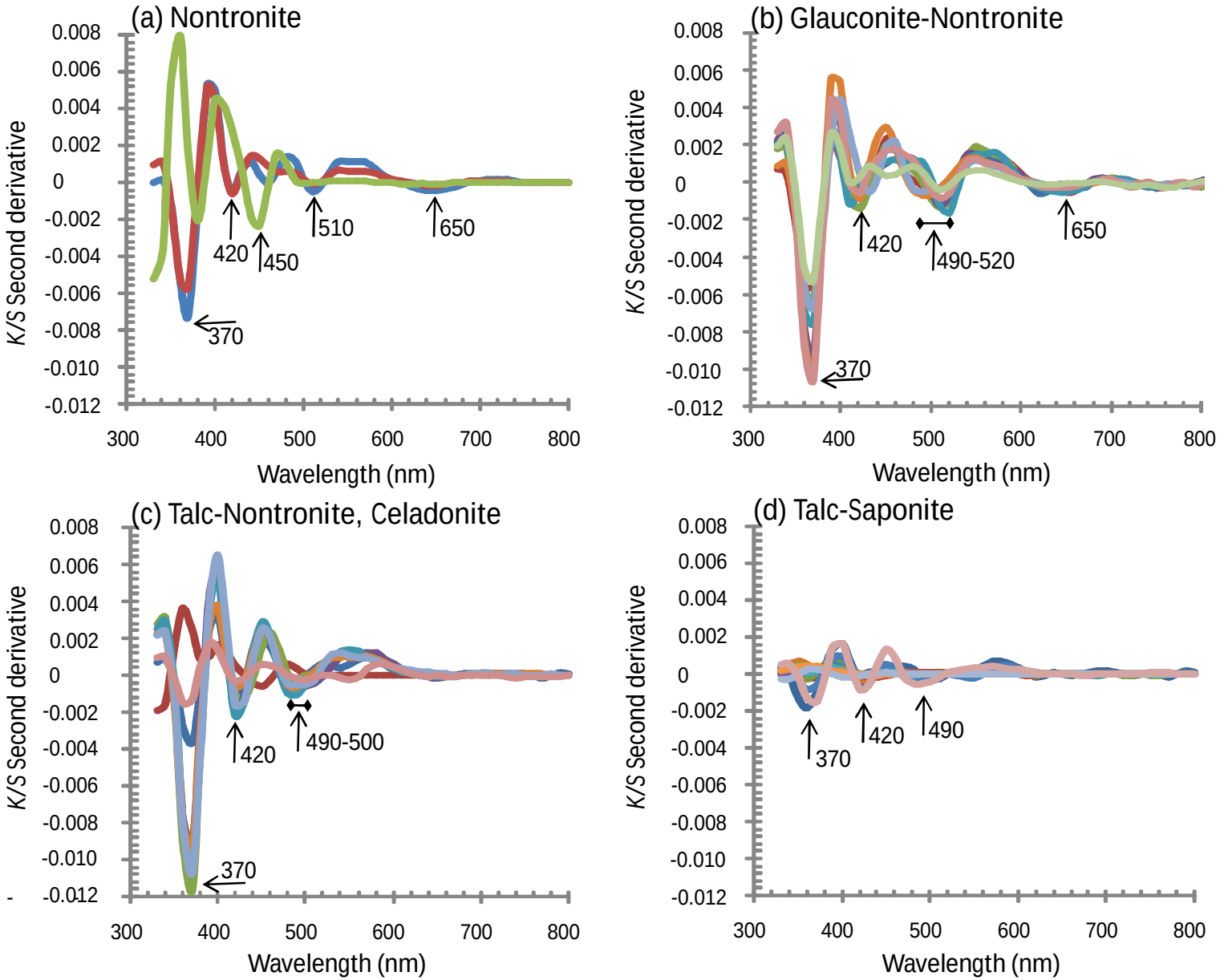
(a) Nontronite
(b) Glauconite-Nontronite
(c) Talc-Nontronite, Celadonite
(d) Talc-Saponite
K/S Second derivative
Wavelength (nm)
0.008
0.006
0.004
0.002
0
-0.002
-0.004
-0.006
-0.008
-0.010
-0.012
300
400
500
600
700
800
370
420
450
510
650
490-520
490-500
490

Figure 2

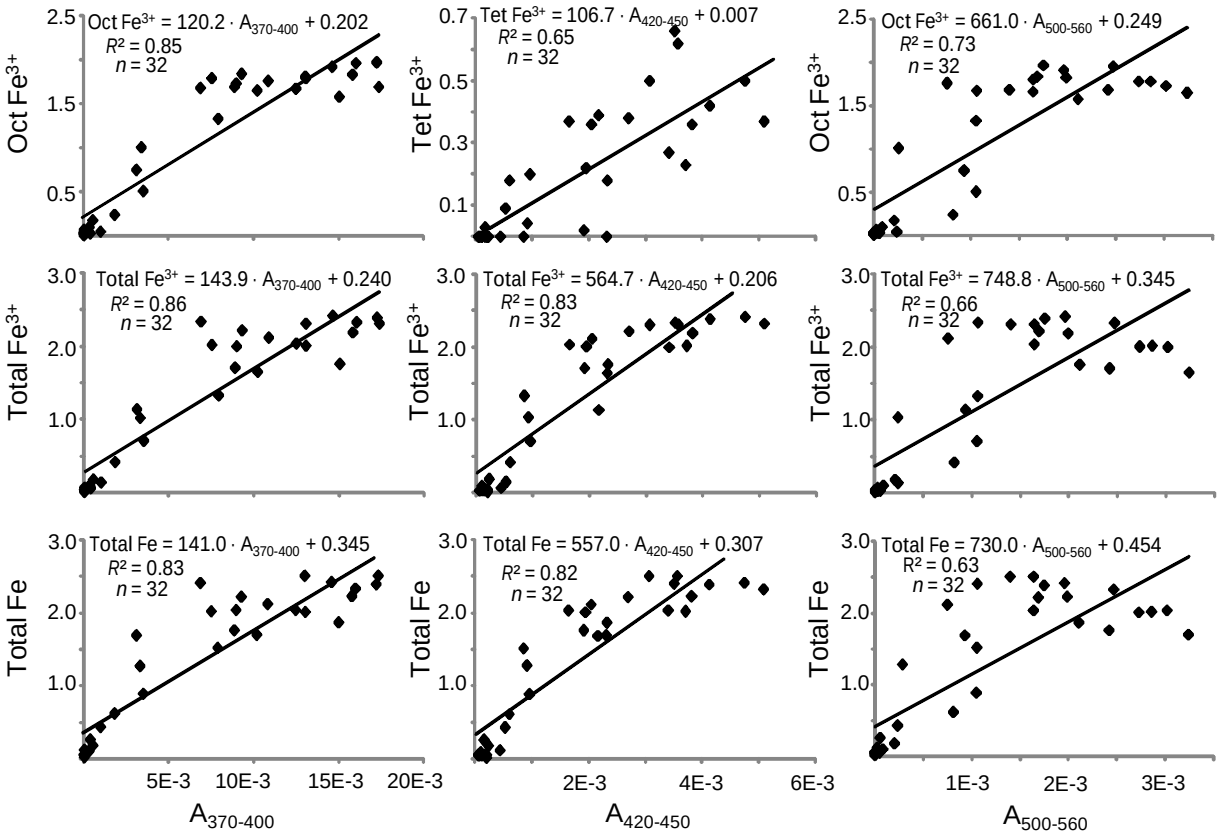
Oct Fe3+ = 120.2 · A370-400 + 0.202
R² = 0.85
n = 32
Tet Fe3+ = 106.7 · A420-450 + 0.007
R² = 0.65
n = 32
Oct Fe3+ = 661.0 · A500-560 + 0.249
R² = 0.73
n = 32
Total Fe3+ = 143.9 · A370-400 + 0.240
R² = 0.86
n = 32
Total Fe3+ = 564.7 · A420-450 + 0.206
R² = 0.83
n = 32
Total Fe3+ = 748.8 · A500-560 + 0.345
R² = 0.66
n = 32
Total Fe = 141.0 · A370-400 + 0.345
R² = 0.83
n = 32
Total Fe = 557.0 · A420-450 + 0.307
R² = 0.82
n = 32
Total Fe = 730.0 · A500-560 + 0.454
R² = 0.63
n = 32
Oct Fe3+
Tet Fe3+
Total Fe3+
Total Fe
A370-400
A420-450
A500-560
5E-3
10E-3
15E-3
20E-3
2E-3
4E-3
6E-3
1E-3
2E-3
3E-3

Figure 3

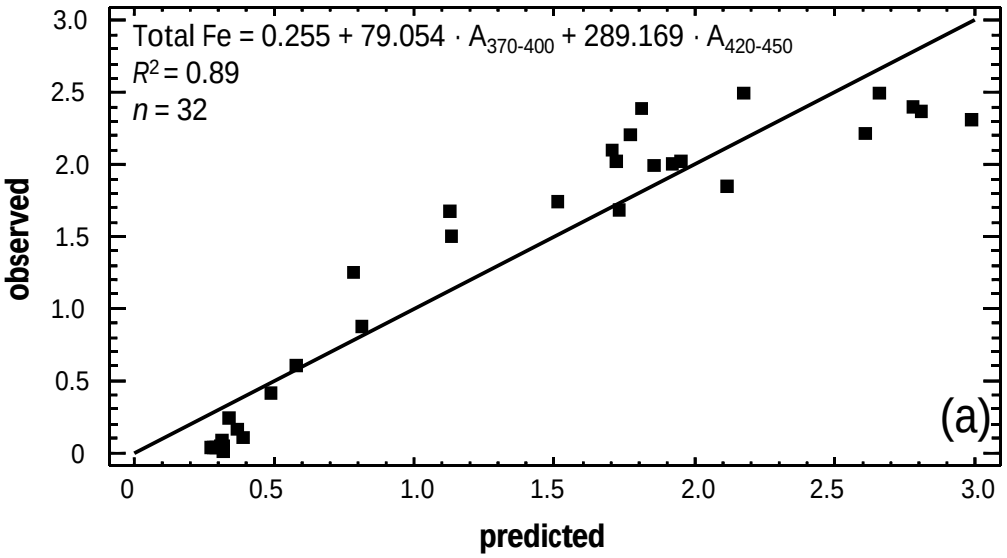
Total Fe = 0.255 + 79.054 · A370-400 + 289.169 · A420-450
R2 = 0.89
n = 32
observed
predicted
(a)
0
0.5
1.0
1.5
2.0
2.5
3.0

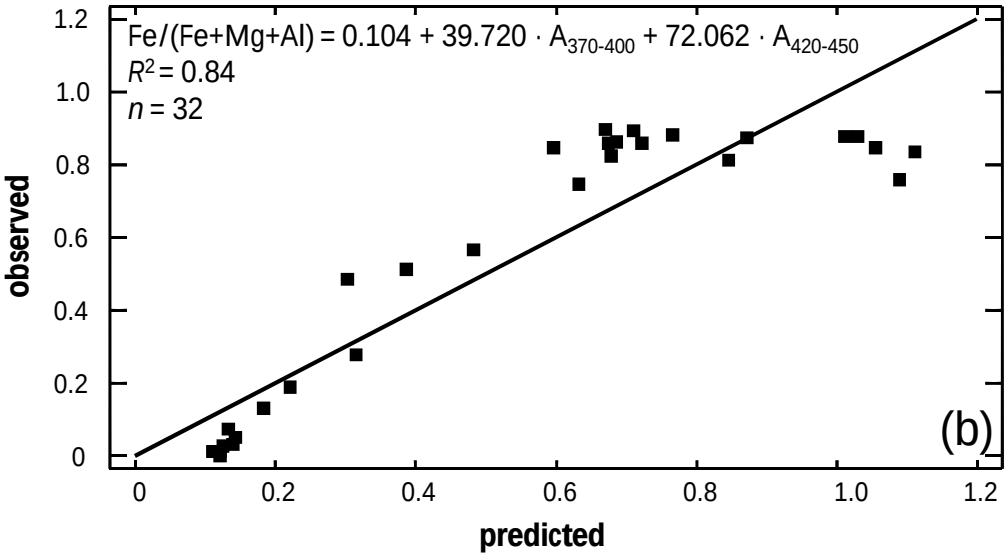
Fe/(Fe+Mg+Al) = 0.104 + 39.720 · A370-400 + 72.062 · A420-450
R2 = 0.84
n = 32
observed
predicted
(b)
0
0.2
0.4
0.6
0.8
1.0
1.2

Figure 4

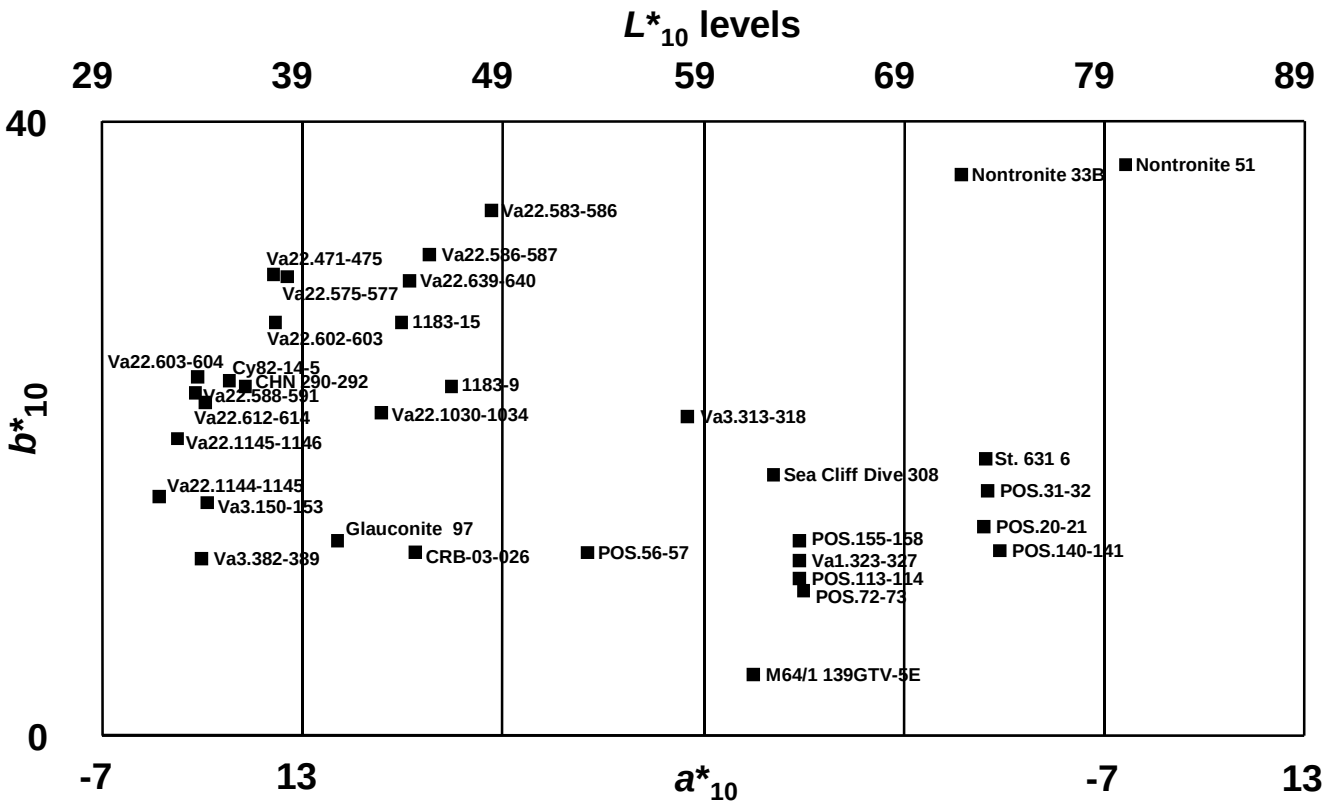
L*10 levels
29
39
49
59
69
79
89
40
0
b*10
-7
13
a*10
-7
13
Nontronite 33B
Nontronite 51
Va22.583-586
Va22.471-475
Va22.586-587
Va22.575-577
Va22.639-640
1183-15
Va22.602-603
Va22.603-604
Cy82-14-5
CHN 290-292
1183-9
Va22.588-591
Va22.612-614
Va22.1030-1034
Va3.313-318
Va22.1145-1146
St. 631 6
Sea Cliff Dive 308
POS.31-32
Va22.1144-1145
Va3.150-153
POS.20-21
Glauconite 97
POS.155-158
POS.140-141
Va3.382-389
CRB-03-026
POS.56-57
Va1.323-327
POS.113-114
POS.72-73
M64/1 139GTV-5E

Figure 5

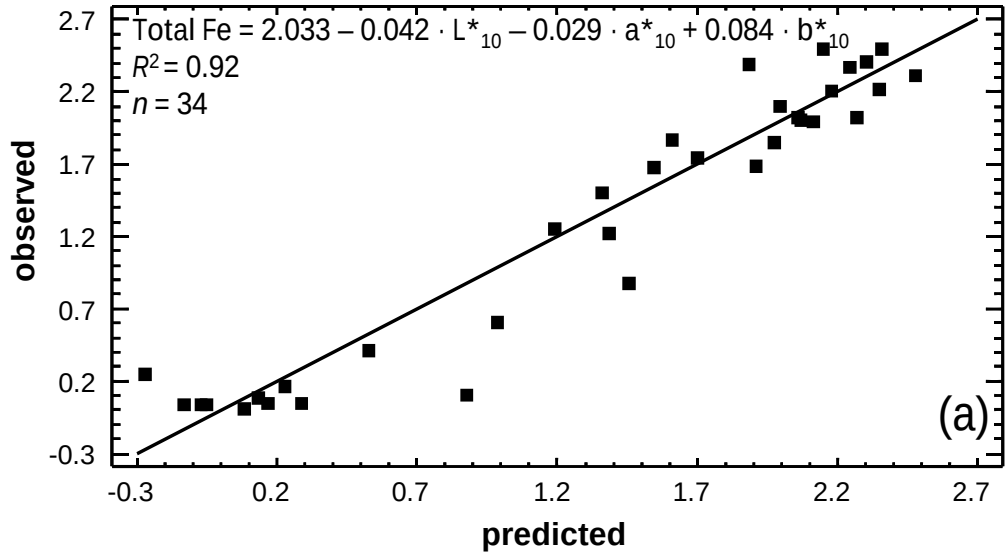
Total Fe = 2.033 – 0.042 · L*10 – 0.029 · a*10 + 0.084 · b*10
R2 = 0.92
n = 34
observed
predicted
(a)
2.7
2.2
1.7
1.2
0.7
0.2
-0.3

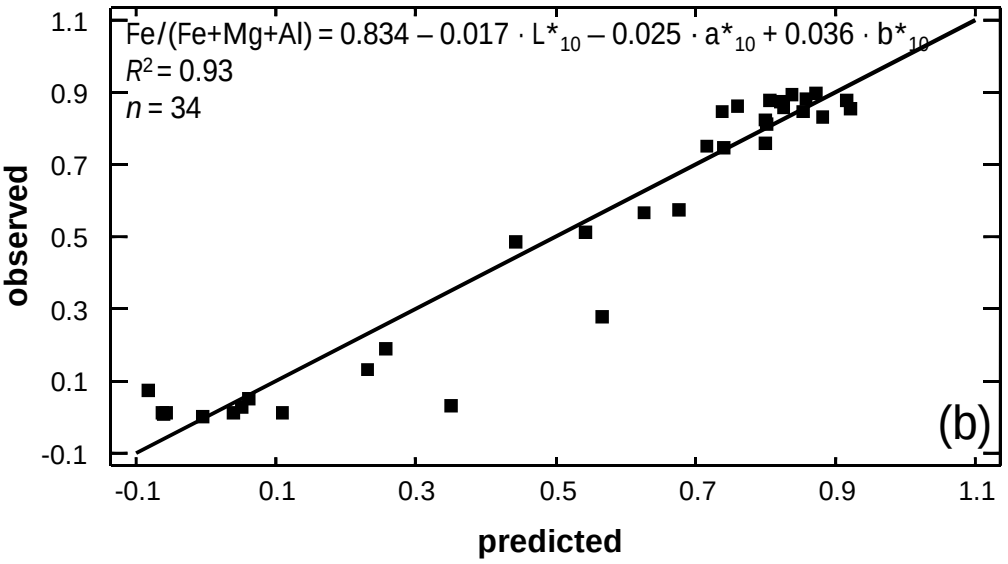
Fe/(Fe+Mg+Al) = 0.834 – 0.017 · L*10 – 0.025 · a*10 + 0.036 · b*10
R2 = 0.93
n = 34
observed
predicted
(b)
1.1
0.9
0.7
0.5
0.3
0.1
-0.1

Figure 6

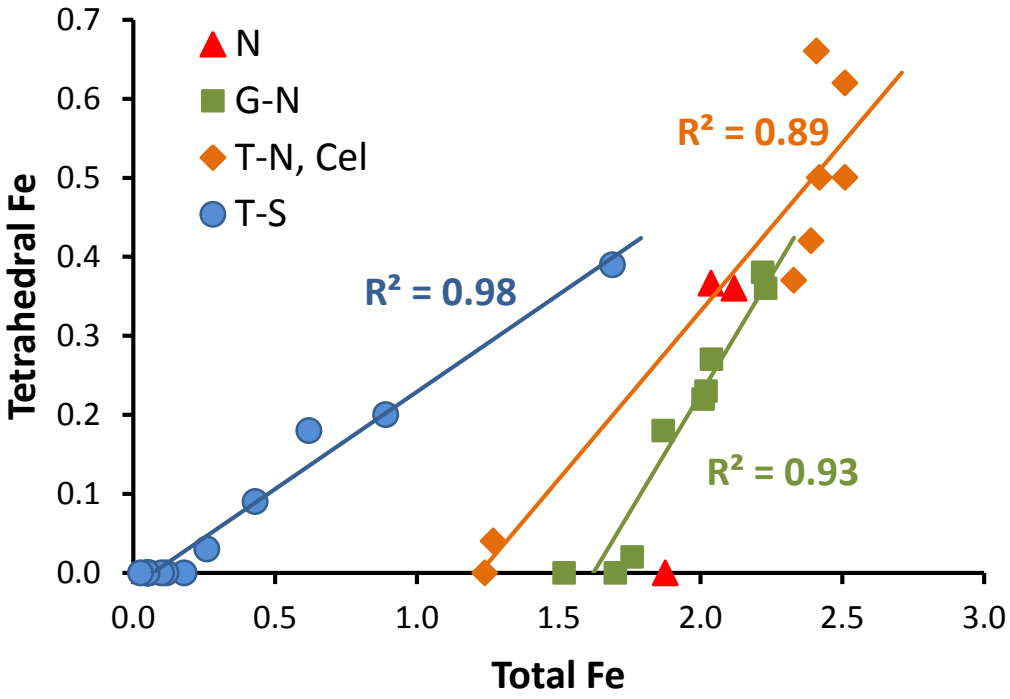
0.7
0.6
0.5
0.4
0.3
0.2
0.1
0.0
Tetrahedral Fe
N
G-N
T-N, Cel
T-S
R² = 0.98
R² = 0.89
R² = 0.93
0.0
0.5
1.0
1.5
2.0
2.5
3.0
Total Fe

Figure 7

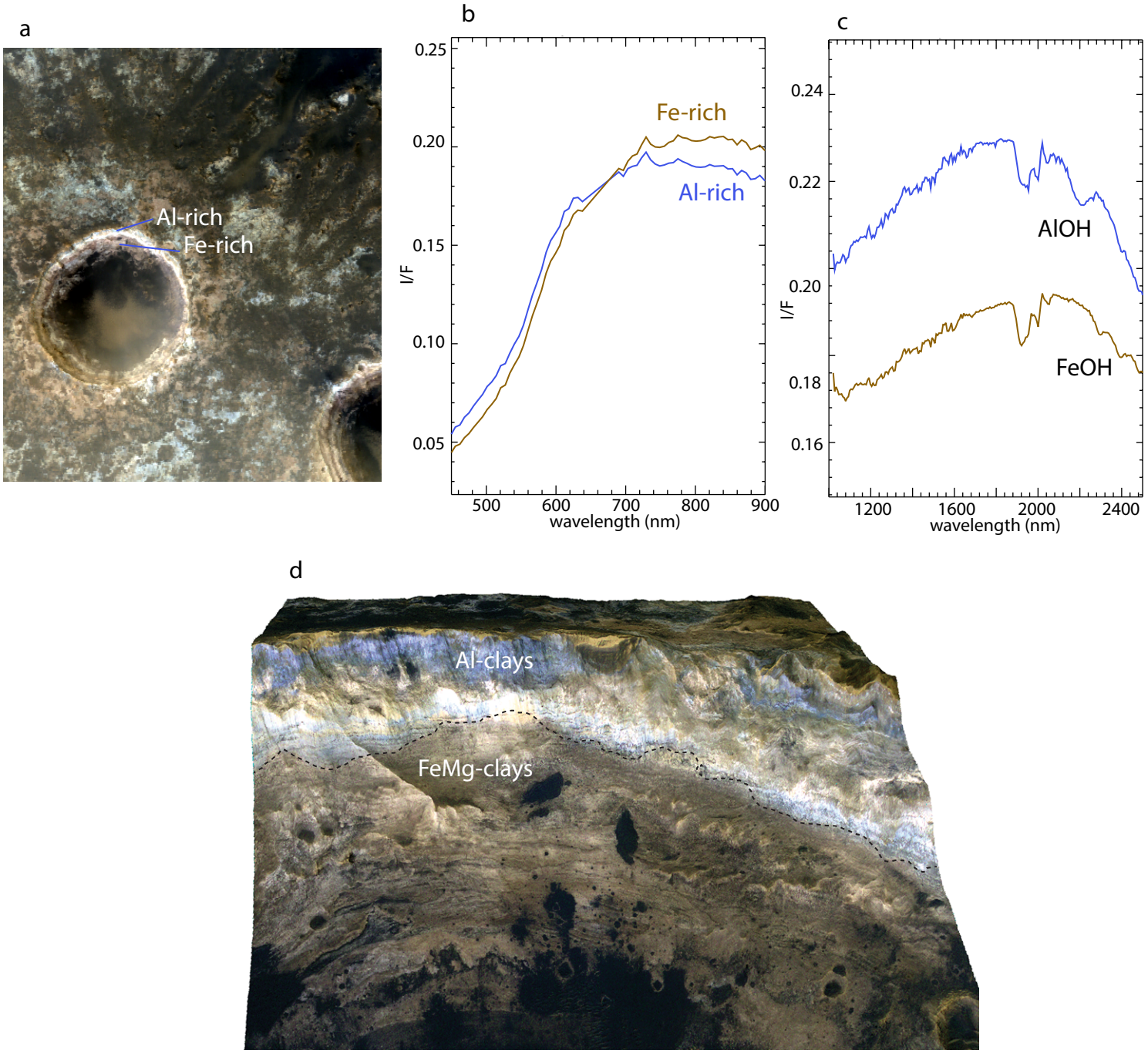
a
Al-rich
Fe-rich
b
Fe-rich
Al-rich
I/F
wavelength (nm)
c
AlOH
FeOH
I/F
wavelength (nm)
d
Al-clays
FeMg-clays

Figure 8

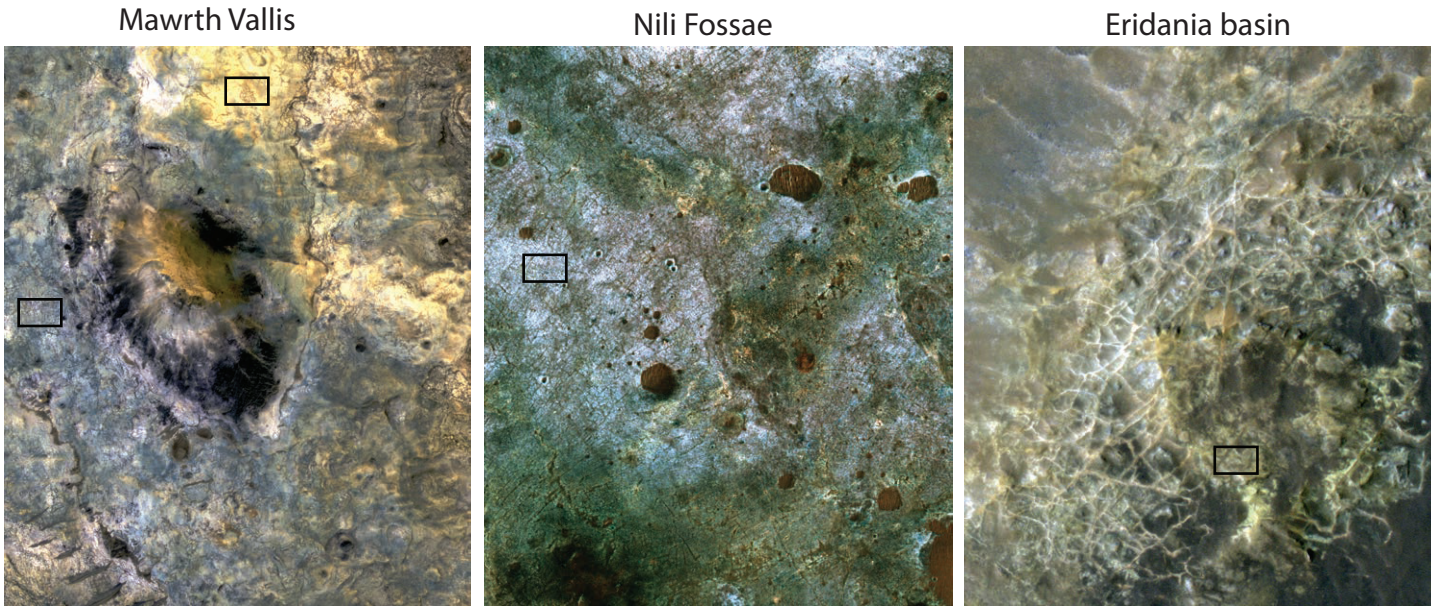
Mawrth Vallis
Nili Fossae
Eridania basin

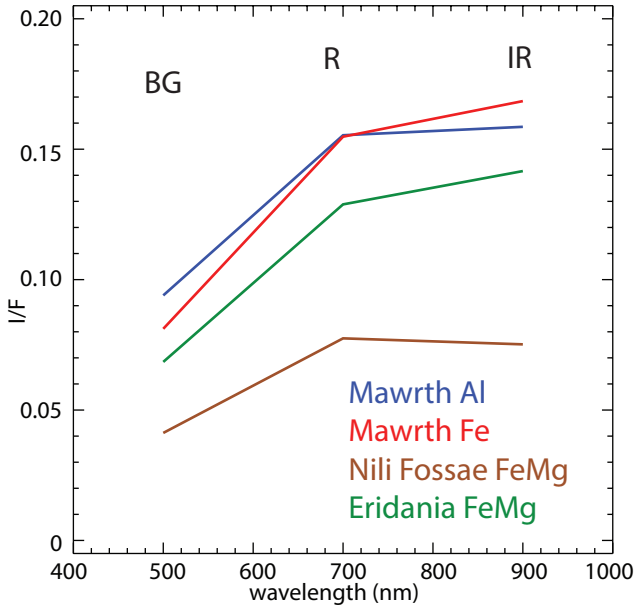
0.20
0.15
0.10
0.05
0
I/F
BG
R
IR
Mawrth Al
Mawrth Fe
Nili Fossae FeMg
Eridania FeMg
400
500
600
700
800
900
1000
wavelength (nm)

Figure 9